

**Performance of the
Demonstrator System
of the future
ATLAS LAr Calorimeter
Trigger Readout**

MASTERARBEIT

zur Erlangung des akademischen Grades

Master of Science

vorgelegt von

Anne-Sophie Reimer

geboren am 08. März 1993 in Zittau

der

TECHNISCHEN UNIVERSITÄT DRESDEN

INSTITUT FÜR KERN- UND TEILCHENPHYSIK
FACHRICHTUNG PHYSIK

FAKULTÄT MATHEMATIK UND NATURWISSENSCHAFTEN

2018

Eingereicht am 05. Juli 2018

1. Gutachter: Prof. Dr. Arno Straessner
2. Gutachter: Prof. Dr. Frank Siegert

Abstract

In 2020, the luminosity of the Large Hadron Collider (LHC) will be more than twice as high compared to the design luminosity. This will lead to an increase of QCD jet background misidentified as high-momentum leptons and photons. However, the trigger system selecting those leptons and photons preferentially, is limited in its bandwidth. This requires an improvement, especially of the Level-1 trigger system. The aim is to record interesting physics events with low transverse energy threshold. Therefore new, so-called super cells shall be read out in the LAr calorimeters. They will have an increased granularity compared to the current trigger readout. Thereby, longitudinal and transverse measurements of the shower shape of a particle will be possible. In parallel to the regular ATLAS main readout, super cell signals were already recorded by a demonstrator system in 2017. By analysing these data, the future shower shape variables are examined and their functionality in the differentiation of electrons and hadronic jets are explored.

Within this thesis, data of the demonstrator readout and the ATLAS main readout are compared. Reconstructed super cell energies will be analysed and different shower shape variables for both readout systems will be investigated. Also, different analyses of pile-up of the demonstrator data are described. Additionally, problems occurring during data taking of the demonstrator system are explained.

Kurzdarstellung

Im Jahr 2020 soll sich die Luminosität des Large Hadron Collider (LHC) im Vergleich zur Design-Luminosität mehr als verdoppeln, was zu einem Anstieg von fälschlich indentifizierten hochenergetischen Leptonen und Photonen aufgrund des erhöhten QCD jet Untergrunds führen könnte. Da das Triggersystem, welches bevorzugt jene Leptonen und Photonen auswählen soll, in seiner Bandbreite jedoch beschränkt ist, erfordert dies eine Verbesserung insbesondere des Level-1-Triggers. Um physikalisch interessante Ereignisse auch mit niedriger Transversalenergieschwelle aufzeichnen zu können, sollen in den LAr-Kalorimetern sogenannte Superzellen ausgelesen werden, die im Vergleich zur bisherigen Auslese eine feinere Segmentierung besitzen. Dadurch wird die Messung der Schauerform eines Teilchens in longitudinaler sowie transversaler Richtung möglich. Parallel zur regulären ATLAS-Datennahme im Jahr 2017 wurden in einem Demonstrationsaufbau Superzellen-Signale aufgezeichnet. Durch die Analyse der aufgezeichneten Daten können Untersuchungen zu den in Zukunft verwendeten Schauerprofilvariablen und zu deren Funktionalität bei der Unterscheidung zwischen Elektronen und hadronischen Jets gemacht werden.

In dieser Arbeit werden die vom Demonstrationsaufbau aufgenommenen Daten mit denen der regulären ATLAS-Datenaufnahme verglichen. Dabei werden rekonstruierte Superzell-Energien betrachtet sowie verschiedene Schauerprofilvariablen für beide Auslesesysteme untersucht und Analysen zu Pile-up anhand der Daten des Demonstrationsaufbaus angestellt. Außerdem werden aufgetretene Probleme bei der Datennahme des Demonstrationsaufbaus beschrieben.

Contents

1. Introduction	1
2. Physical Principles	3
2.1. The Standard Model	3
2.2. Collider physics	5
2.3. Interaction of Particles with Matter	7
3. The Experiment	11
3.1. The Large Hadron Collider	11
3.1.1. Operation of the proton-proton-collider	11
3.1.2. Upgrade Plans	14
3.2. The ATLAS-Detector	15
3.2.1. Structure of the Detector	15
3.2.2. The Trigger System	18
3.3. The Liquid Argon Calorimeter	19
3.3.1. The Detector Structure	19
3.3.2. The Electromagnetic Barrel Calorimeter	20
3.3.3. Signal Processing within the ATLAS Main Readout	21
3.3.4. The Level-1 Trigger	23
3.4. Upgrade of the LAr Calorimeter Trigger System	24
3.4.1. Trigger Electronics	25
3.4.2. Super Cells	26
3.4.3. Shower Shape Variables	29
3.4.4. The Demonstrator	32
4. Analysed Data of the Demonstrator System and the ATLAS Main Readout	35
4.1. Data Samples	35
4.1.1. The ATLAS Main Readout	35
4.1.2. The Demonstrator Readout	38
4.2. Classification of Particle Type	39
4.3. Pulse Peak Sample of the Demonstrator Readout Super Cells	40
4.4. Energy reconstruction of Demonstrator data	43

4.5. Issues with Demonstrator data	45
5. Comparison of Demonstrator and ATLAS Main Readout	49
5.1. Matching of Data	49
5.2. Energy Correlation of the two Readout Systems	51
5.3. Analysis of the Shower Shape Variables	53
5.3.1. R_η - Transverse Energy Ratio	53
5.3.2. f_3 - Shower Depth Variable	54
5.3.3. $\omega_{\eta 2}$ - Shower Width	55
5.3.4. Correlation of the Shower Shape Variables	56
6. Pile-up Studies for the Demonstrator System	59
6.1. Mean Pile-up Energy per Layer	60
6.2. Pile-up Time Spectrum	63
6.3. Pile-up Energy Spectrum	64
7. Summary and Outlook	67
A. Examined Runs	69
B. Mean Pile-up per SC	73
Acronyms	77
Bibliography	81

1. Introduction

Our understanding of the fundamental structure of matter has developed enormously since the foundation of quantum mechanics in the 1930s. The perception of baryons consisting of quarks, the discovery of the positron as an anti-particle, and the discovery of neutrinos are just some of the milestones that have to be mentioned. The Standard Model (SM) [1] is a model of particle physics which describes our achieved understanding of matter very successfully. Nevertheless, there are still questions that could not be answered yet [2]. What are dark matter and dark energy, which make 95 % of our universe? Why do the particles, that we call fundamental by now, have such widely differing masses? What happened at the "big bang"?

The experiments at the LHC aim to get answers to these questions [3]. The LHC with its diameter of 27 km is the largest circular particle accelerator in the world. Here, protons are accelerated and brought to collision, to produce conditions that existed right after the "big bang". At the ATLAS experiment [4], parameters of the SM are matter of research. It is the largest detector at the LHC and a general-purpose experiment. One of its aims is to search for new physics.

In order to gain enough statistics for rare processes in a reasonable time, the beam intensity of the LHC is increased. For this reason, the LHC is subjected several changes and all the detectors have to ensure that data taking is still possible. This requires trigger systems which can cope with high effective collision rates.

This thesis deals with the future Level-1 trigger readout of the electromagnetic calorimeter of the ATLAS detector. The aim is to improve the readout in a way, that recording physical interesting events is still possible with low transverse energy threshold. For that reason, the readout is supposed to get a higher granularity. Therewith, the shower of a particle entering the detector part can be quantified via so-called shower shape variables and information for decision making will improve significantly. In order to examine the future readout, a demonstrator system was installed at the ATLAS detector. In this thesis the readout of the demonstrator was examined and studies about shower shape variables were done.

Due to the increase of the luminosity of the LHC, the average number of interactions raises. This causes an increase of the probability of superposition of signals. Therefore,

1. Introduction

another object of investigation was signal pile-up in the calorimeter.

Chapter 2 describes the fundamental principles of the SM and important parameters of proton-proton colliders. In chapter 3 the LHC, its upgrade plans and the ATLAS detector will be explained. Also a description of the trigger system and the demonstrator are given. The data used for this thesis, their properties and difficulties are described in chapter 4. In chapter 5 the distributions of shower shape variables are discussed for the data of the demonstrator and compared to the data of the ATLAS main readout. Chapter 6 covers pile-up studies with the demonstrator readout. Chapter 7 summarizes the studies of this thesis and gives an outlook.

2. Physical Principles

2.1. The Standard Model

The SM [1] is the most successful model to describe our present understanding of how fundamental particles and three of the four known forces are related to each other. It was developed in the 1970s and describes the electromagnetic, weak and strong interactions; the gravitational force is not included. It is based on the symmetry groups $SU(3)_C \times SU(2)_L \times U(1)_Y$ and it has three conserved quantities. They are called color charge C , hyper charge Y and weak isospin T_3 . By demanding invariance under local gauge transformations additional gauge fields are introduced. Their excitations are described as gauge bosons, which transmit the electro-weak and strong forces.

Each force has at least one gauge boson as force-carrier particle, which all have spin 1. For the strong force, whose symmetry group is $SU(3)_C$, there are eight different gluons, which are massless and carry a pair of color charge (red, green, blue) and anticolor charge (antired, antigreen, antiblue). The range of the strong force is short due to self interaction of gluons.

The symmetry group of the electroweak interaction is $SU(2)_L \times U(1)_Y$. Electromagnetic interactions proceed via photons, which are massless and chargeless. Their range is infinite. The weak force has three force-carriers: the W^+ , W^- and Z^0 . Because they all have a high mass of 80 – 90 GeV, the range of the weak force is comparatively short.

The two types of elementary particles, quarks and leptons, consist of six particles each, which are arranged in pairs, or "generations" (see also figure 2.1). Quarks and leptons are fermions, which means that they have a half-integer spin and obey the Pauli exclusion principle. Quarks interact via all three forces whereas the three charged leptons - electron, muon and tau - do only interact electromagnetically and weakly. The three neutrinos are electrically neutral and interact only weakly.

Quarks do not occur single but as a pair of two (meson) or three (baryon). These so-called hadrons are colorless. The underlying effect is called confinement and is caused by the strong force whose strength increases with the distance of two quarks. When the distance is too large, a quark-antiquark pair emerges from the vacuum,

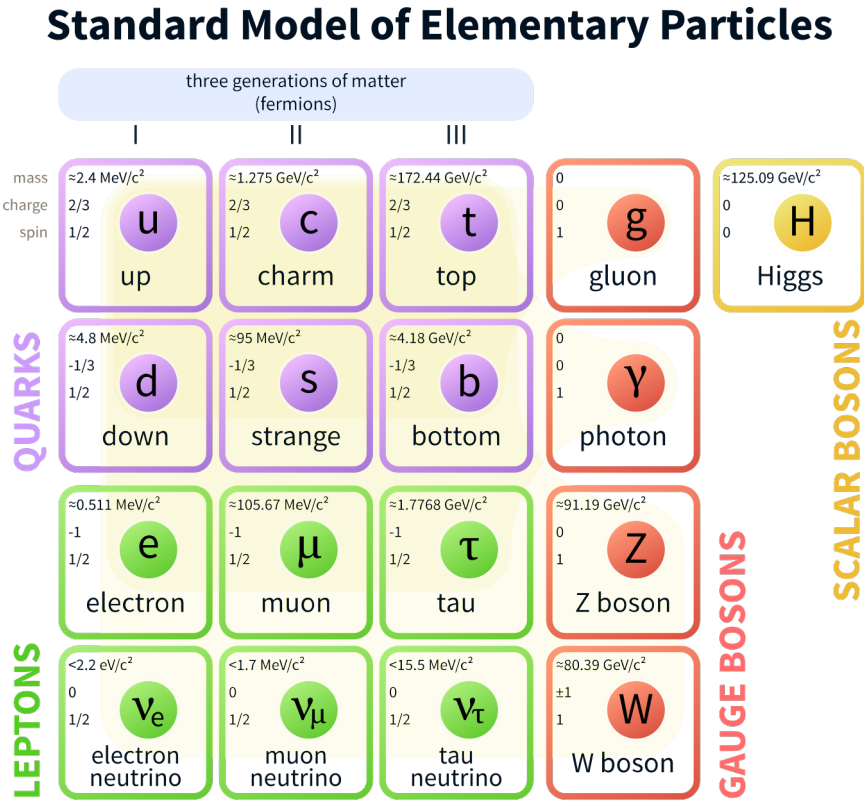


Figure 2.1.: Standard Model of elementary particles [5].

which each bind to one of the initial quarks. This effect is called hadronization and means that quarks are always in a bound, color neutral state. Gluons also do not occur singly. They are always situated in a bound state with at least two quarks. For this reason, cones of hadrons emerge at collisions in particle accelerators. They arise from quarks or gluons which are drifting apart. These particle formations give rise to hadronic jets [6].

A comparatively "new" particle of the SM is the Higgs boson [7, 8]. It is a so-called scalar boson and is an excitation of the Higgs field. Masses of gauge bosons, quarks and leptons are due to their coupling to the Higgs field [9].

Although the SM is very successful, there are still a lot of open issues. The gravitational force is omitted in the theory. Also questions, why there are three generations of quarks and leptons with such a wide-ranging mass scale or how dark matter and dark energy can be described, are not answered by the SM [1, 2]. In order to get more answers for these and many other questions, further experiments are needed to explore the physics beyond the SM [6].

2.2. Collider physics

Particle colliders are a very useful way to analyze elementary particle physics. Accelerated particles are of the simplest kind: electrons, positrons or quarks within protons and antiprotons. At the Large Hadron Collider (LHC) protons (and also heavy ions) are brought to collision. Their collision products provide information about intermediately generated particles with high masses. Some important collider parameters will be introduced below.

Center-of-Mass Energy

A very important collider parameter is the center-of-mass energy \sqrt{s} . It describes the energy which is available in the collision [10]. In the case of colliding beam experiments it can be derived by:

$$\sqrt{s} = \sqrt{\left(\begin{pmatrix} E \\ p_x \\ p_y \\ p_z \end{pmatrix} + \begin{pmatrix} E \\ -p_x \\ -p_y \\ -p_z \end{pmatrix} \right)^2} = \sqrt{\begin{pmatrix} 2E \\ 0 \\ 0 \\ 0 \end{pmatrix}^2} = \sqrt{4E^2} = 2E. \quad (2.1)$$

Figure 2.2 shows a simulation of a proton-proton (pp) collision. Protons are not elementary particles but consist of quarks and gluons. So at a collision these so-called partons collide. From their interactions a variety of particles emerges. Therefore, for parton collisions the reduced center-of-mass energy $\sqrt{\hat{s}}$ is an important parameter:

$$\hat{s} = x_1 x_2 s \text{ with } 0 \leq x_i \leq 1, \quad (2.2)$$

where $x_{1,2}$ are the fractions of momentum for the two colliding partons. For the production of particles with mass M , it is

$$M^2 = \hat{s} \quad (2.3)$$

at lowest order.

Luminosity

An expression for the probability that a certain process occurs is the cross section σ . Therewith we can get the mean number of events N that happen in a time interval dt :

$$\frac{dN}{dt} = \mathcal{L} \sigma. \quad (2.4)$$

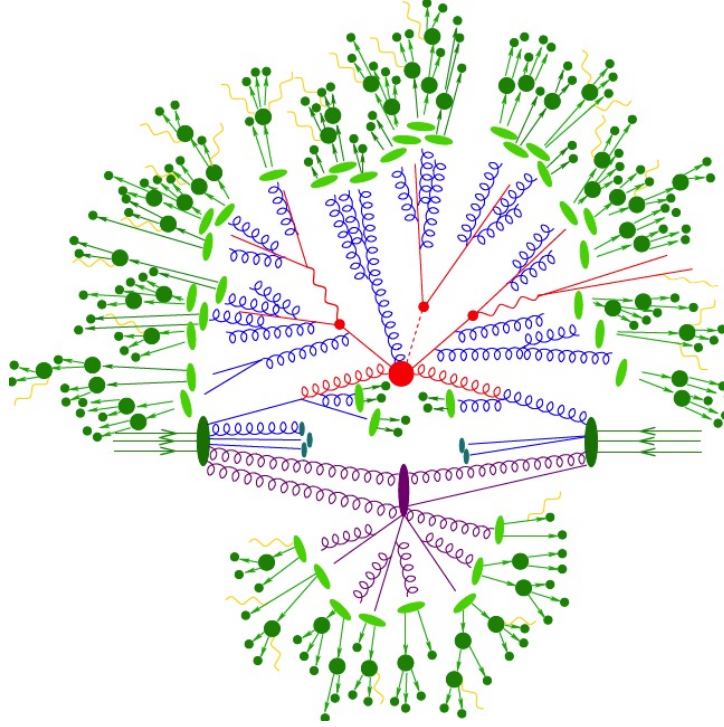


Figure 2.2.: Sherpa collision simulation. Different particles emerge from the initial pp scattering. The "hard" part of scattering is shown in red. Parton showers produce Bremsstrahlung (blue). Multiple "secondary" interactions (purple) and hadronized QCD partons (green) are displayed. Also, unstable hadron decay (dark green) and QED Bremsstrahlung (yellow) are shown.

\mathcal{L} is a proportionality factor and is called instantaneous luminosity. It is an important parameter of particle collider characterization. The integrated Luminosity L describes the number of collisions which take place in a certain time t .

$$L = \int \mathcal{L}(t) dt. \quad (2.5)$$

For the LHC, the instantaneous luminosity can be derived by:

$$\mathcal{L} = \frac{n_b f_n n_1 n_2}{2\pi \sigma_x \sigma_y} F, \quad (2.6)$$

where n_b is the number of proton bunches per beam, f_n is the collision frequency of the accelerator, $n_{1,2}$ contain the number of protons per bunch, $\sigma_{x,y}$ is the horizontal and vertical expansion of the beam and F is the geometric luminosity reduction factor

due to the crossing angle at the interaction point. The design luminosity of the LHC was $10^{34} \text{ cm}^{-2}\text{s}^{-1}$, which was exceeded in 2017 [11].

Figure 2.3 shows the production cross section of different SM processes. The differences in the cross section reach several orders of magnitudes. The inelastic pp scattering has a comparatively large production cross section, which leads to so-called "pile-up" events that are overlayed to interesting physics events like $pp \rightarrow H (+X)$. To increase statistics for finding rare processes at particle colliders, it is desired to have a high luminosity [12, 13].

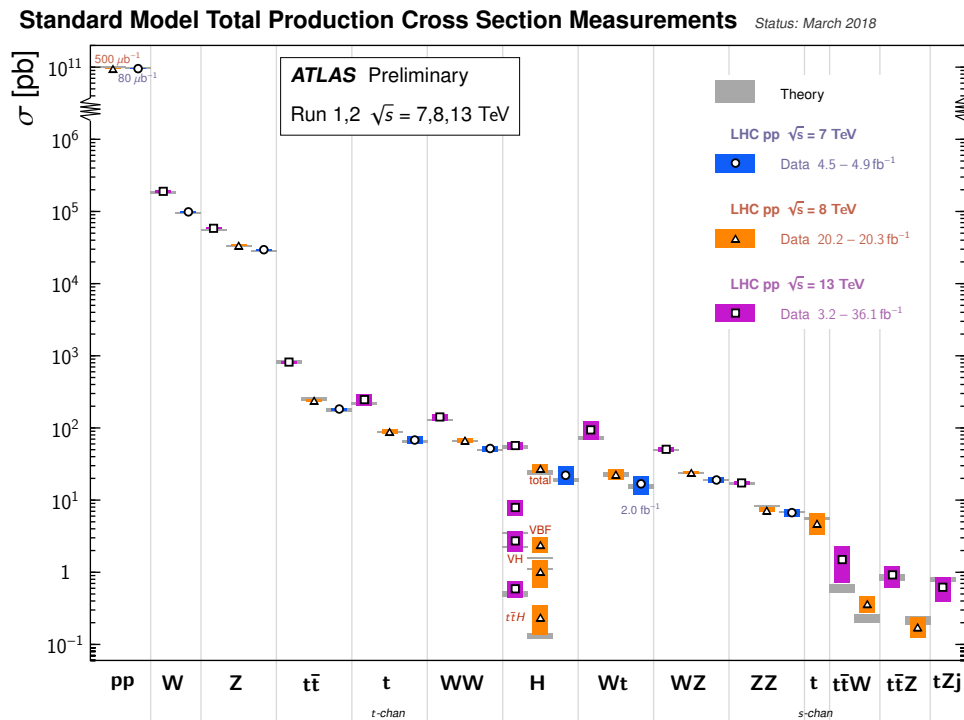


Figure 2.3.: Summary plot of several SM total production cross section measurements and the corresponding theoretical expectations [14].

2.3. Interaction of Particles with Matter

At pp-collisions a vast variety of particles can emerge. Depending on the achieved center-of-mass energy in the collider, also heavy particles like Z^0 , W^\pm or Higgs bosons can occur. Even though these particles are existing too short to detect them directly, their decay products like for example photons, electrons, muons, taus and hadronic

2. Physical Principles

jets can be measured. For some selected particles their interaction mechanisms with matter will be described below.

Electrons and photons interact electromagnetically. At high energies, electrons do Bremsstrahlung, where photons are emitted. Electrons with low energy primarily scatter with the atoms in the detector material and ionize or excite these (see figure 2.4). High energy photons produce electron-positron pairs. The emerging positrons lose their energy by scattering with the detector material and finally recombine with an electron which results in two photons with an energy of 511 keV. Photons with low energies do Compton scattering and interact via the photoelectric effect (see figure 2.5). Both particle types build electromagnetic showers in the calorimeter material of a detector, which result from the alternating formation of electrons and photons [15]. Figure 2.6 illustrates this process.

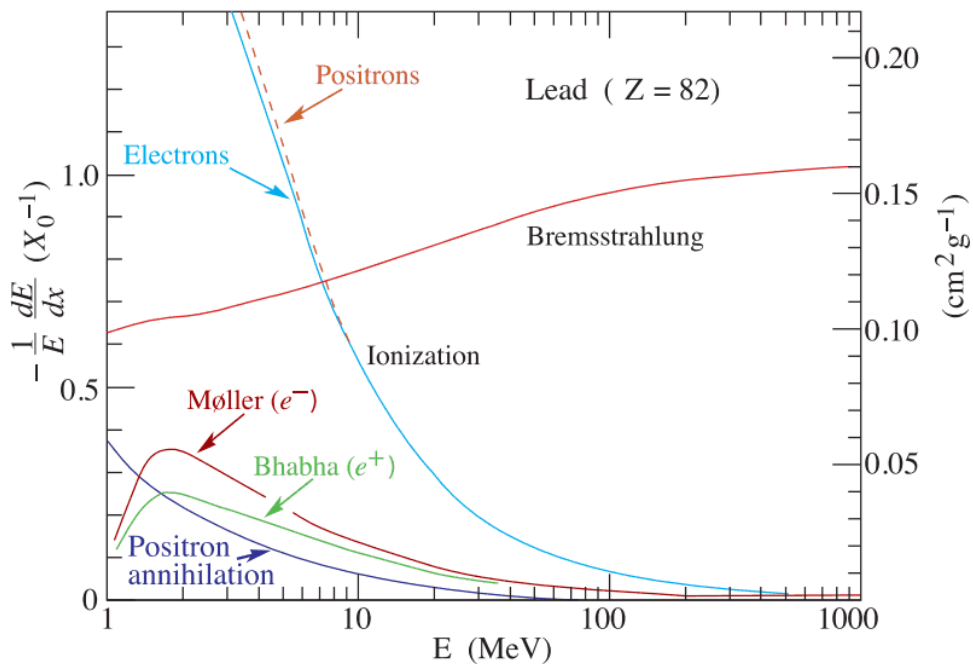


Figure 2.4.: Energy loss per radiation length of electrons in lead [16], which is the main absorbing material in the barrel and endcap region of the ATLAS LAr calorimeters.

Jets interact hadronically. Entering the detector material a spectrum of secondary particles emerges, which have a vast variety of interactions. The interaction processes are mainly inelastic interactions with nuclei and their description is very complex [18]. Pions are the most common interaction results. Neutral pions decay to pairs of photons and cause electromagnetic showers within the absorbed jet. This is one reason, why hadronic particles always deposit energy also in the electromagnetic part of a calorimeter.

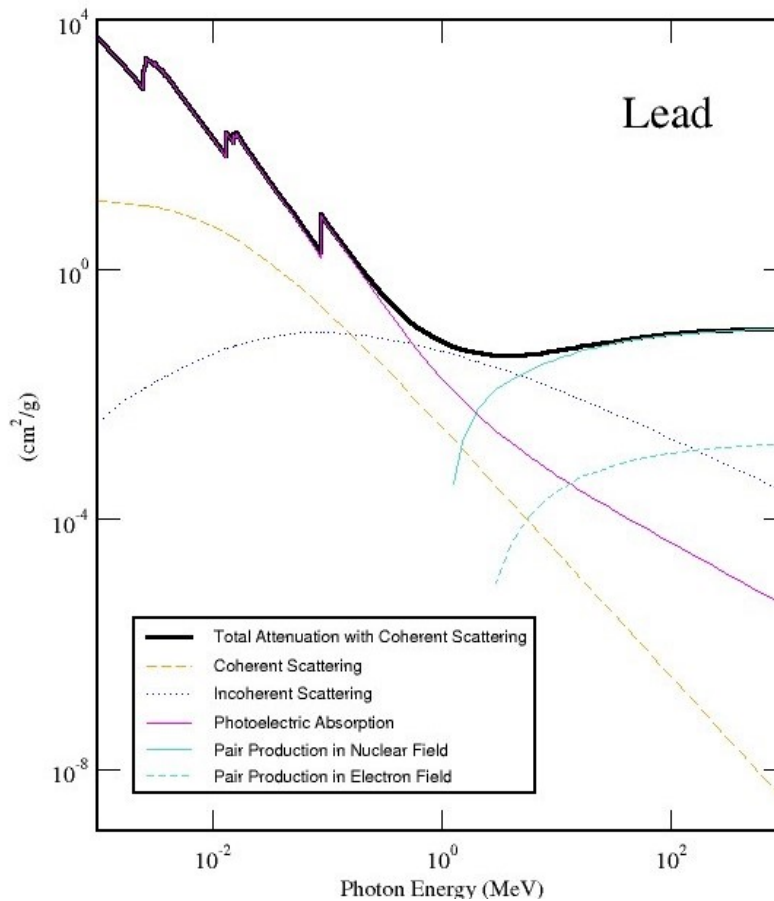


Figure 2.5.: Attenuation of photons in lead [17], which is the main absorbing material in the barrel and endcap region of the ATLAS LAr calorimeters.

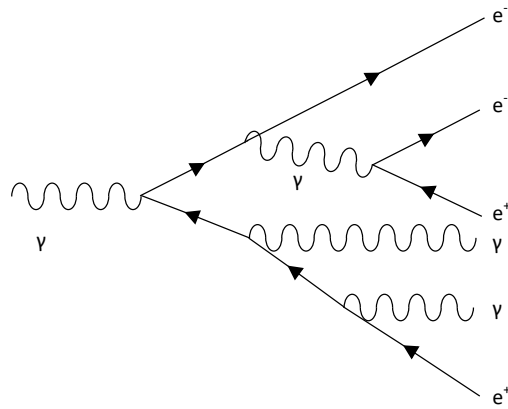


Figure 2.6.: Illustration of the shower formation of a photon.

3. The Experiment

3.1. The Large Hadron Collider

The Large Hadron Collider (LHC) at CERN is a pp (or heavy ion) collider and the biggest particle accelerator in the world. It is located in a 27 km tunnel at a depth between 45 m and 170 m on the French-Swiss border, near Geneva. There are two separate beam pipes in which protons or heavy ions are accelerated in opposite directions and four points where they are brought to collision. The detectors A Toroidal LHC Apparatus (ATLAS) [4], Compact Muon Solenoid (CMS) [19], Large Hadron Collider beauty (LHCb) [20] and A Large Ion Collider Experiment (ALICE) [21] are located at these points. Figure 3.1 shows a scheme of the CERN complex with the LHC and the various preaccelerators [3].

3.1.1. Operation of the proton-proton-collider

The LHC was designed for reaching a maximum centre-of-mass energy for pp-collisions of $\sqrt{s} = 14$ TeV with an energy of 7 TeV per beam. The accelerated protons are kept on their tracks by 1232 superconducting dipole magnets, which generate magnetic fields up to 8.3 T and need to be cooled to 2 K [3]. The beam pipes need to be highly evacuated, since the protons would scatter with the gas molecules. 16 radio-frequency cavities accelerate the protons. Electromagnetic fields are used to create a resonance in which the charged protons feel an accelerating force. Therefore, the beam is not filled continuously but with bunches of protons [23]. A further structure of the proton bunches is introduced by the kicker magnets, which transport the beam from one accelerator to the next one until the beam is injected into the LHC.

3. The Experiment

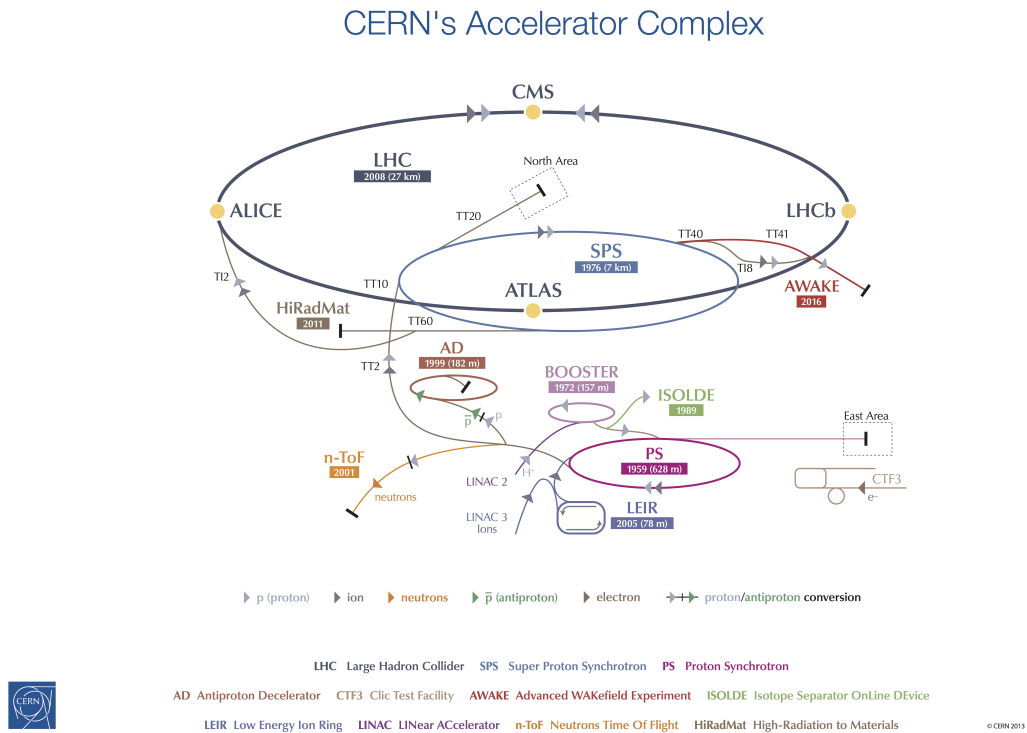


Figure 3.1.: Scheme of the CERN complex. Preaccelerators and detectors of the LHC are displayed [22].

Bunch Trains

At the LHC, the bunch crossing rate is 40 MHz, which means that every 25 ns bunches cross. There are 3564 possible bunches in the LHC, which are identified by the so-called Bunch Crossing Identification (BCID) number. Bunches do not have to be filled, they can also be empty. The LHC has different filling schemes of its bunches. A group of filled bunches is called bunch train and usually consists of 72 filled bunches. An example of such a scheme for the ATLAS detector is displayed in figure 3.2. As can be seen, there are different settings for a Bunch Crossing (BC). The two crossing bunches can be:

- "paired": both beams are filled with protons
- "unpaired": just one beam is filled with protons
- "empty": neither beam is filled.

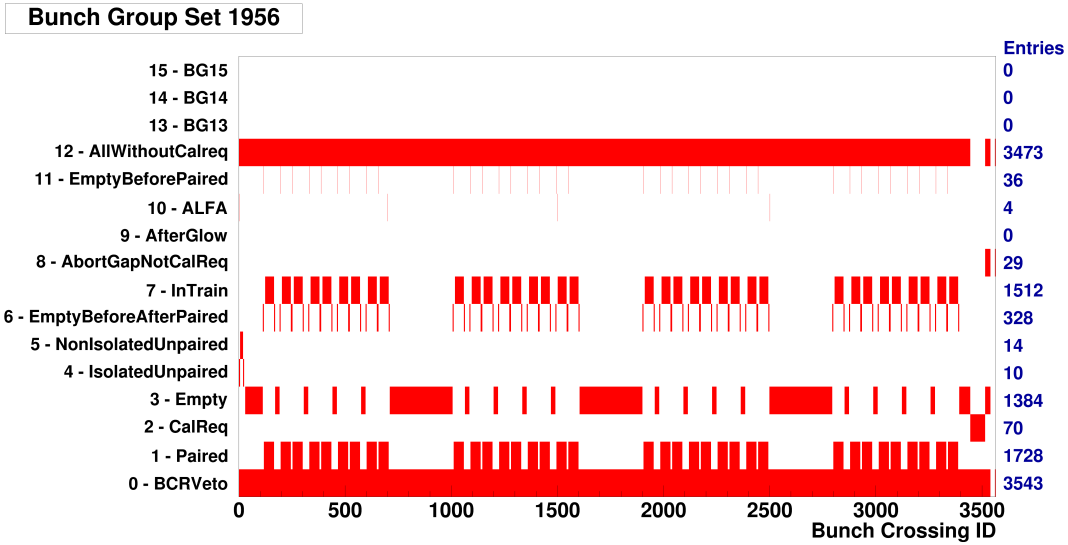


Figure 3.2.: Bunch group set for the LHC [25]. Red bars display BCs fulfilling the criteria listed on the left.

Also there exist additional defined crossings for special purposes [24].

Pile-up

Every 25 ns, bunches with up to 1.15×10^{11} protons per bunch cross at the LHC. So, when several protons collide at one BC, interaction products of different particle collisions can cause signals in the detector. This can result in the superposition of two signals of different collisions, which is called pile-up. There are three different types of pile-up.

Event pile-up describes events, where the particle collision of interest is accompanied by further particle collisions at the same BC. The overlaid collision may deposit energy in the same readout channel. In-time pile-up means the superposition of signals of different pp-interactions within the same BC. Here, the energy deposition takes place in the same readout channel, so that the energies of the different particles cannot be differentiated easily. The superposition of signals from different BCs is called out-of-time pile-up. Here, additional pp-collisions occur in BCs right before or after the collision of interest. Since a signal pulse exceeds the time interval between two BCs, this leads to overlaid signals [26].

3. The Experiment

3.1.2. Upgrade Plans

In figure 3.3 the timeline of the LHC is displayed. For developing and extending the physics program, during the phases of shutdown, the LHC is subjected several changes, whereas during the runs, new data is collected [28].

- **Run 1:** During the first run period of the LHC, data taking was very successful. 75 % of the design luminosity was achieved and a center-of-mass energy of 8 TeV. The average number of interactions per BC was $\langle\mu\rangle \sim 20$.
- **Long Shutdown 1 (LS1):** In 2013 to 2015 in terms of the Phase-0 upgrade, machine elements such as magnet splices were repaired. Also the collimation scheme was upgraded in order to reach design luminosity and energy.
- **Run 2:** In 2016 the LHC reached its design peak luminosity of $\mathcal{L} = 10^{34} \text{ cm}^{-2} \text{ s}^{-1}$ and a collision energy of 13 TeV.
- **Long Shutdown 2 (LS2):** The Phase-1 upgrade includes improvements of the preaccelerators and injector complex, and the insertion of new cryogenic plants. This is expected to double the luminosity compared to Run 2.
- **Run 3:** In this period, the instantaneous luminosity will be expected to increase twofold to threefold compared to nominal. This will lead to an annual integrated luminosity of $\sim 300 \text{ fb}^{-1}$. The average number of interactions per BC is expected to be $\langle\mu\rangle \sim 60$.

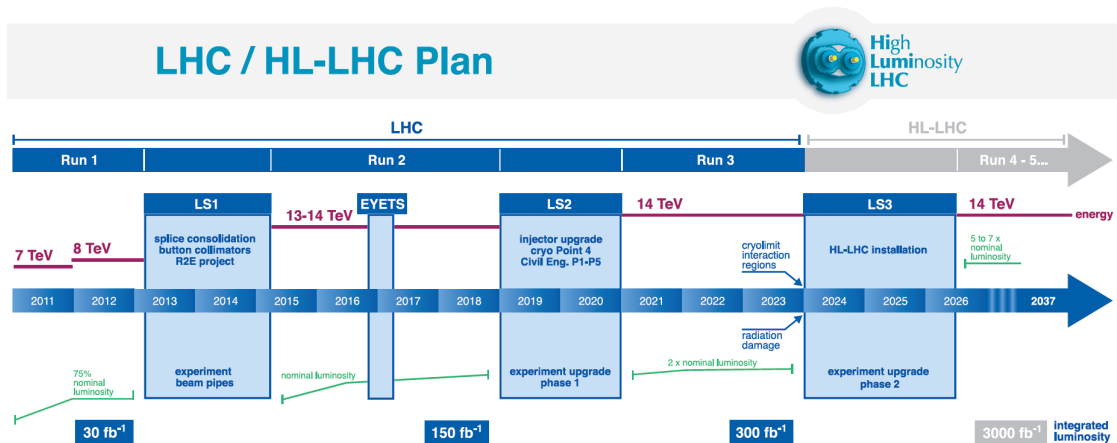


Figure 3.3.: Overview of upgrade plans of the LHC in the period from 2011 to 2026. Data is collected during the runs. In the period of long shutdown (LS) improvements for the accelerator and detectors are done [27].

- **Long Shutdown 3 (LS3):** In 2024 to 2026 the LHC will be prepared to reach a nominal Luminosity of $\mathcal{L} = 5 * 10^{34} \text{ cm}^{-2}\text{s}^{-1}$.
- **HL-LHC:** From 2026 for the High Luminosity LHC, an annual integrated luminosity of 250 fb^{-1} is planned.

3.2. The ATLAS-Detector

The ATLAS experiment is a general-purpose particle physics experiment. Its main purposes are precision measurements of SM parameters and the search for physics beyond the SM [29]. To understand the huge mass differences of the SM particles within the Higgs mechanism is one important subject of interest. The verification of the Higgs boson in 2012 was a landmark in this context [7].

3.2.1. Structure of the Detector

The ATLAS detector has a spherical structure around the interaction point, where the protons of the two beam pipes are brought to collision. With its weight of 7000 tons and dimensions of $25 \text{ m} \times 25 \text{ m} \times 44 \text{ m}$, it is the largest detector of the four main LHC experiments. Three major parts characterize it. As seen in figure 3.4, these are the inner detector, the calorimeters and the muon spectrometers [4].

Inner Detector

The inner detector is the part that lies closest to the interaction point. It begins a few centimeters from the beam axis and extends to a radius of 1.2 meters. A magnetic field, created by a solenoid magnet, penetrates the detector and causes charged particle tracks to curve. Their interactions with the material make it possible to track them and to reconstruct their trajectory. Information on charge and momentum of the particle can thus be measured.

The inner detector has three parts. The innermost is the Pixel Detector, then a Semiconductor Tracker follows and the Transition Radiation Tracker (TRT) builds the outermost component.

3. The Experiment

Calorimeters

Beyond the inner detector, the calorimeters are situated. The electromagnetic calorimeter lies innermost, the hadronic calorimeter outermost. Both serve for absorbing particles and by that for the reconstruction of their energies. Whereas the electromagnetic calorimeter absorbs particles that interact electromagnetically, the hadronic calorimeter does the same with particles that interact via the strong force.

Muon Spectrometer

The Muon Spectrometer is a tracking system for muons. Superconducting toroid magnets cause particle tracks to be bent so that their momenta can be measured. It consists of separate trigger and high-precision tracking chambers.

Figure 3.5 shows the tracks of common particles. Due to their various properties and interaction mechanisms, one can distinguish different particle types. Whereas charged particles like electrons and muons deposit parts of their energy along the whole track, for example photons are not visible until they reach the electromagnetic calorimeter.

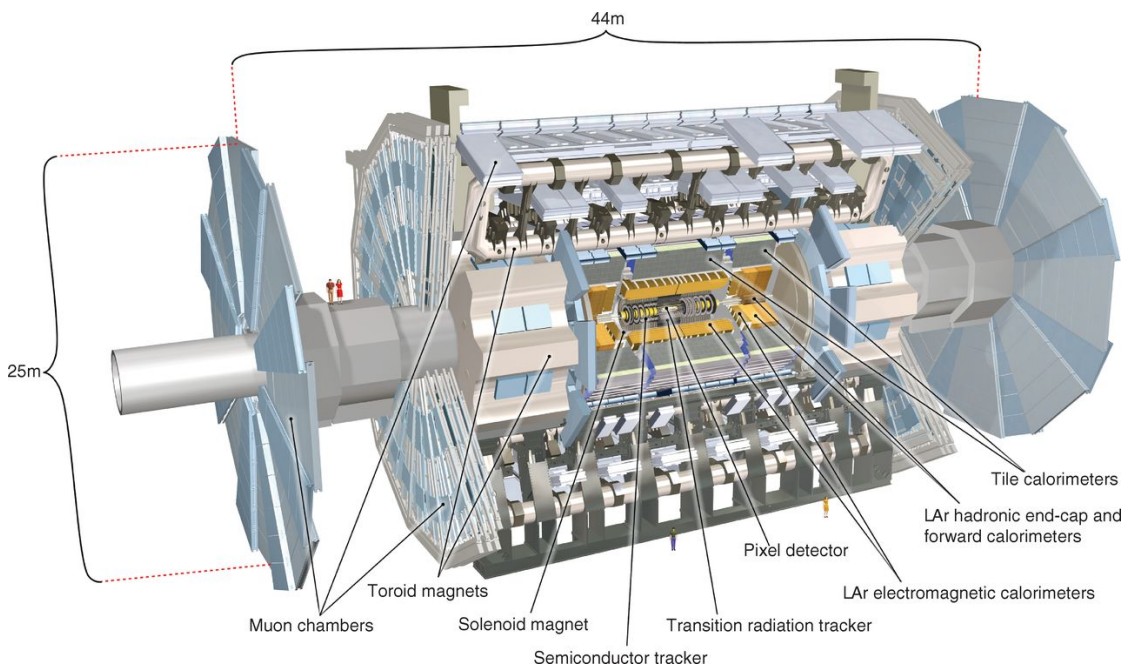


Figure 3.4.: Structure of the ATLAS detector [30].

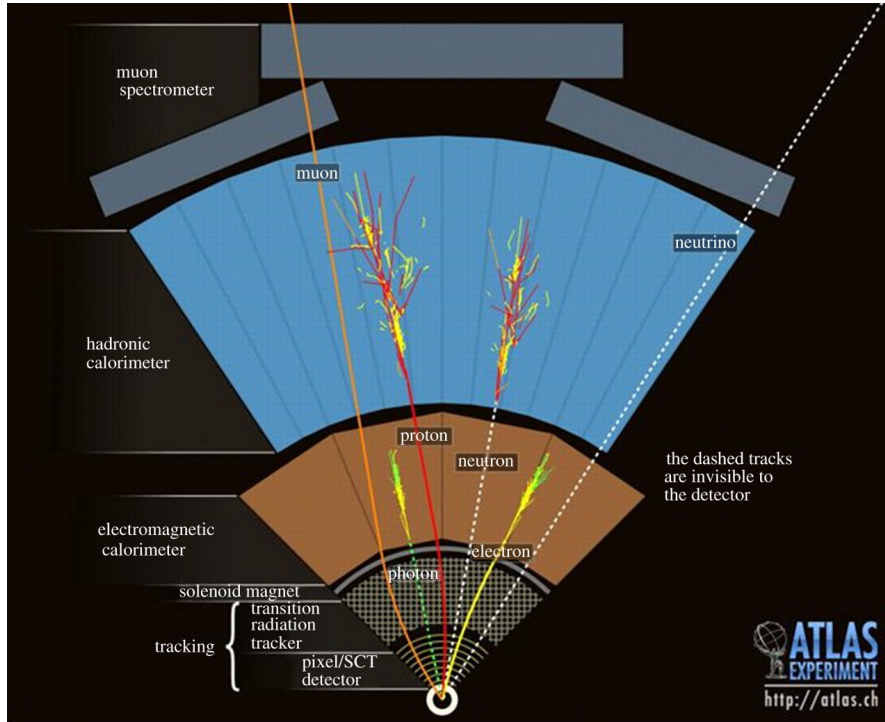


Figure 3.5.: Illustration of tracking particles in the ATLAS detector [31].

Coordinate system

To determine the positions and directions of particle tracks and detector elements, ATLAS uses a right-handed coordinate system with its origin in the interaction point. The x -axis points to the center of the LHC, the y -axis points up and the z -axis points along the beam pipe anti-clockwise.

Since the detector is spherical, it has turned out that spherical coordinates are more useful. The azimuthal angle ϕ is measured in the x - y plane around the beam axis proceeding from the x -axis. The polar angle θ proceeds from the beam axis and is converted to the pseudorapidity

$$\eta = -\ln(\tan(\theta/2)). \quad (3.1)$$

Differences in η are Lorentz invariant under boosts along the y -axis and therefore, in case of pp collisions, where partons are responsible for the hard scattering, it is more useful than θ [4].

The angular distance between two detector points can then be calculated by

$$\Delta R = \sqrt{(\Delta\eta)^2 + (\Delta\phi)^2}. \quad (3.2)$$

Transverse Variables

Since protons are not elementary particles, their partons collide when the former are brought to collision. The interaction point of the partons and their rest frame is not known a priori (but can be reconstructed in certain cases). Therefore, it is not possible to know the initial energy that contributed to the reaction. This is the reason, why transverse variables are introduced. They are defined in the x - y -plane transverse to the beam axis. The assumption is, that the momentum of the protons transverse to the beamline is zero. Thus, the sum of the transverse momentum of the particles, which are produced by the reaction, must be zero as well because of momentum conservation. If there is a strong deviation from zero, there has been a particle that has not been detected [32].

The transverse momentum is Lorentz-invariant under shifts along the beam axis and derived by:

$$p_T = \sqrt{p_x^2 + p_y^2} = |\vec{p}| \cdot \sin\theta. \quad (3.3)$$

The transverse energy is

$$E_T = E \cdot \sin\theta. \quad (3.4)$$

Another important variable is the missing transverse energy E_T^{miss} . It is the energy that is not deposited in the detector, i.e. from the particles that do not interact with the detector material, e.g. neutrinos. The E_T^{miss} is calculated from the energy flow of all other detected particles:

$$\begin{aligned} \vec{E}_T^{miss} &= \sum_n \begin{pmatrix} E_T \times \cos\phi_n \\ E_T \times \sin\phi_n \end{pmatrix} = \begin{pmatrix} E_{x,n} \\ E_{y,n} \end{pmatrix}, \\ E_T^{miss} &= |\vec{E}_T^{miss}| = \sqrt{\left(\sum_n E_{x,n}\right)^2 + \left(\sum_n E_{y,n}\right)^2}. \end{aligned} \quad (3.5)$$

3.2.2. The Trigger System

During Run 2 the ATLAS detector has a maximal data recording rate of 1 kHz. Since the collision rate is 40 MHz, a trigger system is necessary. For this purpose, ATLAS uses a two stage trigger system [4].

The first trigger stage is the Level-1 (L1) trigger. It is based on hardware and takes data from the calorimeters and muon chambers. If an event can pass, a Level-1 accept

(L1A) signal is released together with the Region of Interest (ROI) of the interesting event. In the L1 buffer, the detector information is retained, until the event is accepted via the L1A. If this happens, the data are transferred to the Readout Drivers (ROD)s and further to the Data Acquisition (DAQ) system. Here, they are stored in local buffers. The maximum L1A rate, which the detector readout systems can cope with, is 100 kHz. The latency limit is $\approx 2.5 \mu\text{s}$ [33, 34].

The second trigger stage is the so-called High Level Trigger (HLT). It is a software system with a Level-2 (L2) and Event Filter stage. The L2 trigger partially reconstructs the event based on the ROI. In the Event Filter, data based on the full detector resolution are processed in regions selected by the L2. Also data of the tracking system are used. It makes the final trigger decision. For the HLT the maximum trigger rate is 1 KHz with a processing time of 300 ms [34].

With increasing trigger level it takes more time to make a trigger decision because of algorithms getting more complicated. If a trigger accepted an event, information that were gained are transferred to the next trigger step and further investigations take place. If after all three trigger steps the event stays interesting, the buffered data in the DAQ system are moved to the permanent storage at the CERN computer centre [4].

3.3. The Liquid Argon Calorimeter

Figure 3.6 shows a sketch of the Liquid Argon (LAr) Electromagnetic (EM) calorimeter [35] of the ATLAS detector. The calorimetry system covers a region within $|\eta| < 4.9$ for energy deposition and consists of different parts which are all symmetrical in ϕ . In order to measure the energy of a particle, it needs to be completely absorbed.

3.3.1. The Detector Structure

The ATLAS calorimeters are sampling calorimeters, which means that they consist of layers with an absorbing material and layers with an active material. A particle that reaches the absorbing material will interact with it, generate secondary particles and slow down. This leads to a cascade of particles that builds a shower in the detector material. LAr is used as active medium in the Electromagnetic Barrel Calorimeter (EMB), Electromagnetic Endcap Calorimeter (EMEC), Hadronic Endcap Calorimeter (HEC) and Forward Calorimeter (FCal). Secondary particles passing through the LAr cause ionized argon atoms and electrons that drift to the electrodes and create a signal.

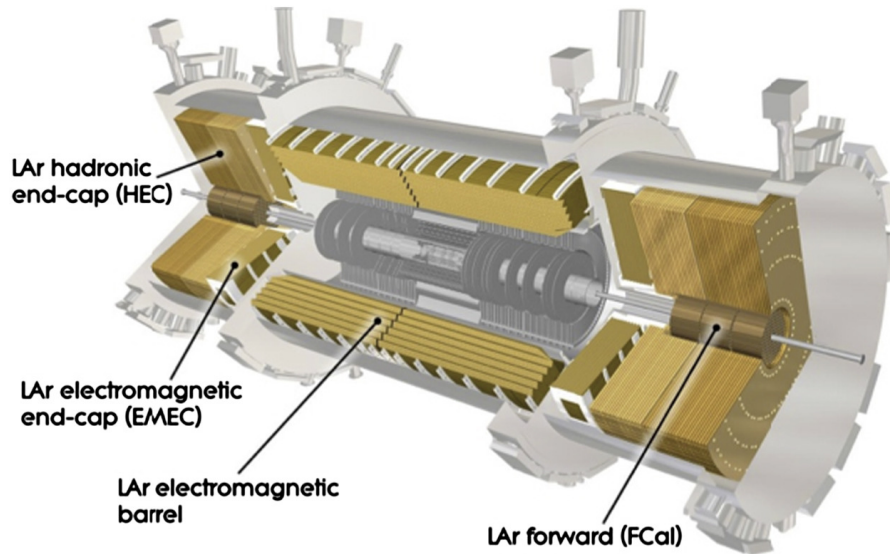


Figure 3.6.: LAr Calorimeter of the ATLAS detector [30].

Summing up the measured energy within the calorimeter cells will give the initial energy of the particle using the known sampling fraction. The EMB will now be described in more detail.

3.3.2. The Electromagnetic Barrel Calorimeter

The EMB is the part of the LAr calorimeter that is located centrally around the interaction point within $-1.475 < \eta < 1.475$. Its absorbing material is lead.

As it can be seen in figure 3.7, the EMB is separated into four layers: the presampler, front, middle and back layer. The accordion geometry enables full ϕ coverage without cracks in between the module edges [36]. The front layer has a very fine segmentation in η direction. This makes it possible to divide between photons with a small angle in between that originate from a pion decay or directly from the pp-collision. Since the middle layer has the largest extent, here, the most energy is deposited. In the back layer, the energy of the tail of an electromagnetic shower is deposited. Figure 3.7 also shows the size of the elementary cells in the different parts of the EMB. For the data acquisition readout each cell's signal is read separately - in total 109 568 channels [4].

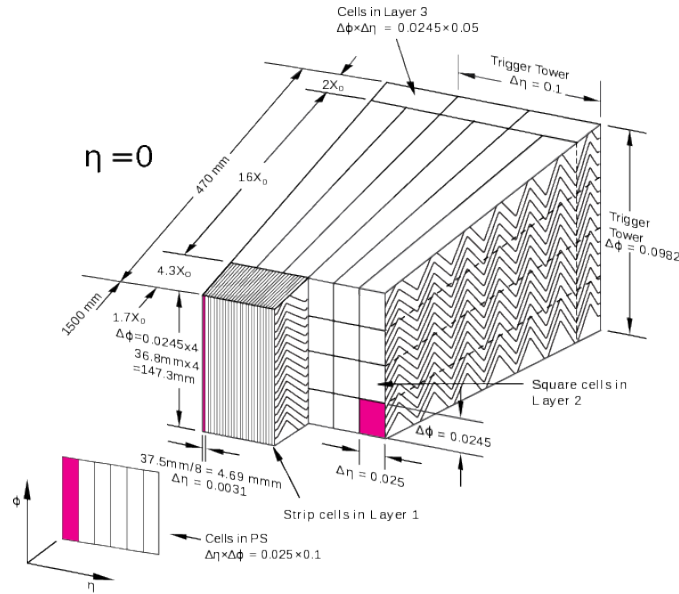


Figure 3.7.: Scheme of the structure of the EMB for $|\eta| = 0$ [35]. There are four different layers which have different granularity: the presampler (PS or layer 0), the front layer (layer 1), the middle layer (layer 2) and the back layer (layer 3). The expansion of the layers is displayed in terms of the radiation length. Also the accordion geometry of the absorbing and active material is visible.

3.3.3. Signal Processing within the ATLAS Main Readout

Signals coming from the calorimeter cells have a triangular form with a length of 300 – 600 ns (see figure 3.8). The pulse heights are proportional to the energy deposits of the particle, which caused the ionization in the calorimeter cells.

The Front End Boards (FEBs) receive these analogue signals, sample and digitize them. First, the signal gets amplified and split into three gain scales with the ratio 1/10/100. Next, it is shaped in order to optimize the signal-to-noise ratio. This is done by a CR-(RC)² analogue filter, where the single differentiation step removes the long tail from the signal and the two integrations limit the bandwidth, which serves for noise reduction. The resulting signal has a bipolar shape with a shifted peak and an undershoot of about 20 % of the peak amplitude (see figure 3.8). Next, the signal is sampled by the Switched Capacitor Array (SCA) with 40 MHz, which is the LHC bunch crossing frequency, and stored until the L1 trigger makes its decision.

If the L1 trigger accepted the event, the signal is digitized by a 12 bit Analog-to-Digital Converter (ADC). Four samples per channel and the optimal gain scale are read out

3. The Experiment

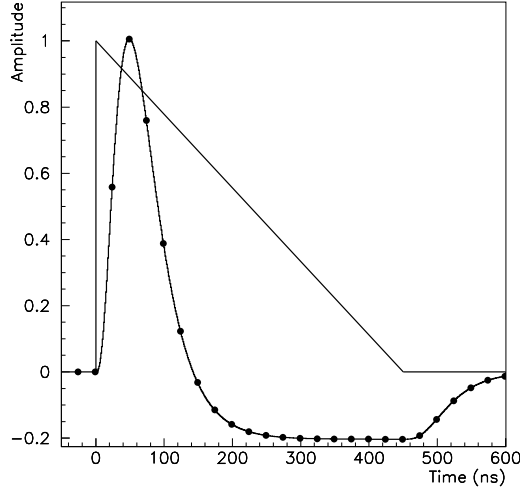


Figure 3.8.: The triangular detector pulse of an elementary cell in the LAr EMB is displayed. The signal is shaped and the resulting characteristic bi-polar form is sampled every 25 ns [4].

and sent to the Readout Drivers (RODs) at the back end electronics via an optical link. For each calorimeter channel and each L1 trigger, the optimal readout gain is chosen by a gain-selector chip. The required 16 bit precision for the whole energy range is reached by the 12 bit digitization in combination with the gain selection procedure.

At the back end electronics, the ROD system, the trigger, timing and control (TTC) and the L1 trigger receiver is located. At this point, data from the front-end electronics are read, digitally processed and finally transmitted to the DAQ system. Each ROD processes the signals of 1024 detector cells. This also includes the application of an optimal filtering algorithm, which optimizes the signal-to noise ratio further. The ROD boards calculate energy, time and quality of a detector pulse. These information are sent to the DAQ, where the collection of data fragments and event-building is performed. There, also recording takes place.

If an event was selected by the event filter, it is moved to the storage at the CERN computer center. The event filter processing task classifies the events to the ATLAS-defined data streams: electrons, muons, jets, photons, E_T^{miss} , τ -leptons, and B -physics. Depending on the stream classification, the event is recorded in one or more files [4, 37].

3.3.4. The Level-1 Trigger

The L1 trigger receives data from the calorimeter and the muon chambers, as already mentioned. It consists of the Level-1 calorimeter trigger (L1Calo) trigger, the muon trigger and the Central Trigger Processor (CTP). Figure 3.9 shows a scheme of the L1 trigger. Object of study are muons, electrons, photons, jets, and τ -leptons decaying into hadrons with high transverse momentum, or large missing or total transverse energy [4].

Whereas the L1 muon trigger is based on signals from the muon trigger chambers, the L1Calo considers about 7000 so-called Trigger Towers (TTs) from the EM and hadronic calorimeters. For TTs, the energy is summed up over all calorimeter cells in an area of $\Delta\eta \times \Delta\phi = 0.1 \times 0.1$ and over all layers. The trigger decision and L1A is made by the CTP which combines all the information from the L1Calo trigger and the muon trigger, and decides based on so-called trigger menus. These are programmed with up to 256 distinct trigger items, which include different combinations of required input data [4, 38].

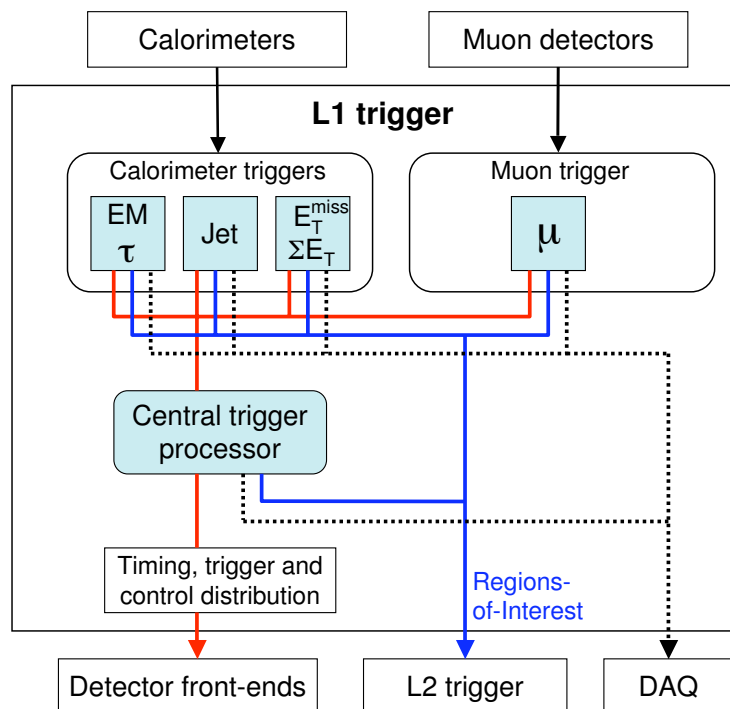


Figure 3.9.: Block diagram of the L1 trigger [4].

The L1Calo has three subsystems: the Pre-Processor (PP), the Cluster Processor (CP) and the Jet/Energy-sum Processor (JEP). The PP digitizes the analogue input signals and associates them with their BC. Then, data are transferred to the CP and the JEP in parallel. At the CP, electron, photon, and τ -lepton candidates with a transverse energy above a certain threshold and fulfilling isolation criteria are identified. At the JEP, it is searched for jets and global sums are produced to find missing transverse energy. Both processors use so-called sliding-window filter algorithms, which do feature searches on overlapping, sliding clusters of summed TTs. These information are transmitted to the CTP.

3.4. Upgrade of the LAr Calorimeter Trigger System

For the future operation of the ATLAS detector in Run 3, up to $\langle\mu\rangle = 60$ pile-up events with an instantaneous luminosity of $3 \times 10^{34} \text{ cm}^{-2}\text{s}^{-1}$ are expected. During Run 1 the peak number of pile-up events was $\langle\mu\rangle \sim 20$. Due to the constraints in granularity, bandwidth and latency at the L1 trigger, an increase in trigger thresholds would be necessary to cope with this. The ATLAS readout dead time leads to a limited event rate at the L1 trigger of 100 kHz. Since interesting events with energies beyond the threshold would be discarded, the aim is to avoid an increase of the threshold of the LAr calorimeter trigger to remain sensitive to physics at the electroweak energy scale ($p_T = 20 \text{ GeV}$) [36].

Therefore, a higher granularity trigger readout of the ATLAS LAr calorimeters is foreseen in the Phase-1 upgrade. Two new modules, the electromagnetic Feature Extractor (eFEX) and the Jet Feature Extractor (jFEX) will be installed and will work in parallel to the JEP and CP initially (see figure 3.10). The function of the eFEX is to search for electron, photon and τ -lepton candidates. At the JEP jet, large-area τ , missing transverse energy and the total energy are object of interest. For more information see [39]. Because of the higher granularity readout, it is possible to use more complex algorithms in order to identify particles. The use of so-called Shower Shape Variables (SSVs) will be described in section 3.4.3.

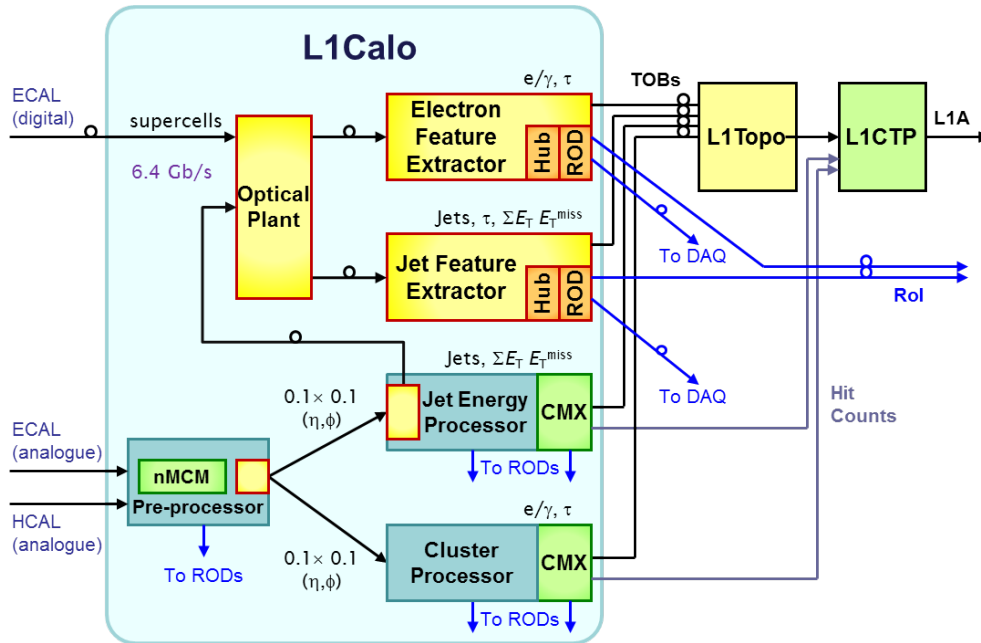


Figure 3.10.: Scheme of system architecture for the future L1 trigger during Run 3 [39]. New components are shown in yellow and orange.

3.4.1. Trigger Electronics

To enhance the trigger feature extraction and background rejection is one goal of the future system, that digitizes the detector signals. The readout will be divided into 34000 so-called Super Cells (SCs), whose signals will be digitized at 40 MHz with a 12 bit precision. The segmentation of the calorimeter trigger readout with SCs compared to with TTs will therefore be increased by 10. The data is transferred via optical links to a digital processing system, which will extract the energies of the SCs [36]. During LS2 in 2018, new trigger readout electronics will be installed.

Figure 3.11 shows the readout electronics of the current (blue) and the future (red) upgraded system.

In the current readout system for gaining the L1A, the signals of the calorimeter cells are summed to form TTs and sent to the calorimeter trigger. Summing is done by three systems: by the shaper chips, the Layer Sum Board (LSB) located on the FEB and by the Tower Builder Board (TBB). The still analogue summed signal is passed on to the trigger receivers. Here, gain differences among the channels are equalized. Finally the signal is transferred to the L1Calo digitizer system and after the trigger decision is made, the L1A signal is possibly sent [36].

3. The Experiment

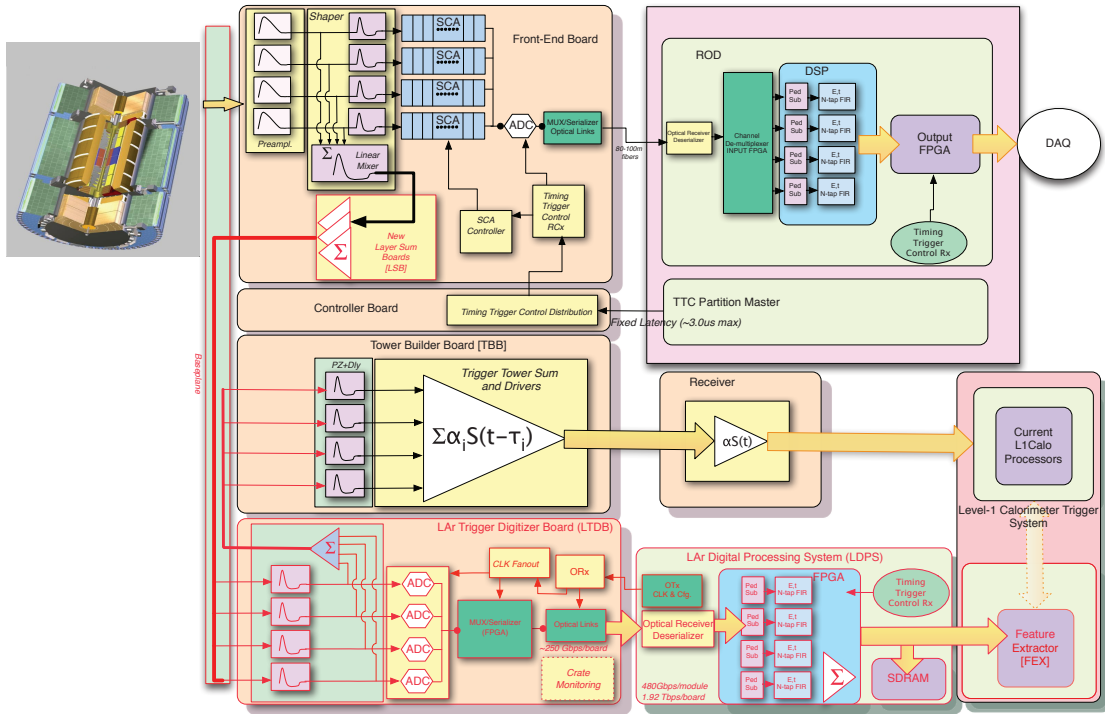


Figure 3.11.: Architecture of the future readout system of the LAr calorimeter [28]. New components of the readout are displayed in red.

In the upgraded system, instead of the TT signals, a new LSB will form SC signals which are then transferred over the Front End Crate (FEC) to the new LAr Trigger Digitizer Board (LTDB). The SC signals are transformed with a 12 bit ADC at 40 MHz and sent to the back end electronics via optical fibers. At the LAr Digital Processing System (LDPS) the deposited transverse energy of the particle shower is calculated, assigned to the correct BC and sent to the L1A calorimeter system, where the L1A signal is generated.

For Run 3 the previous analogue and upgraded digital system will work simultaneously. This is why the new LSB and the new LTDB will both take part in performing the TTs.

3.4.2. Super Cells

In the following, the dimensions of the SCs will be described. Figure 3.12 visualizes the translation from one TT consisting of 60 calorimeter cells to 10 SCs.

3.4. Upgrade of the LAr Calorimeter Trigger System

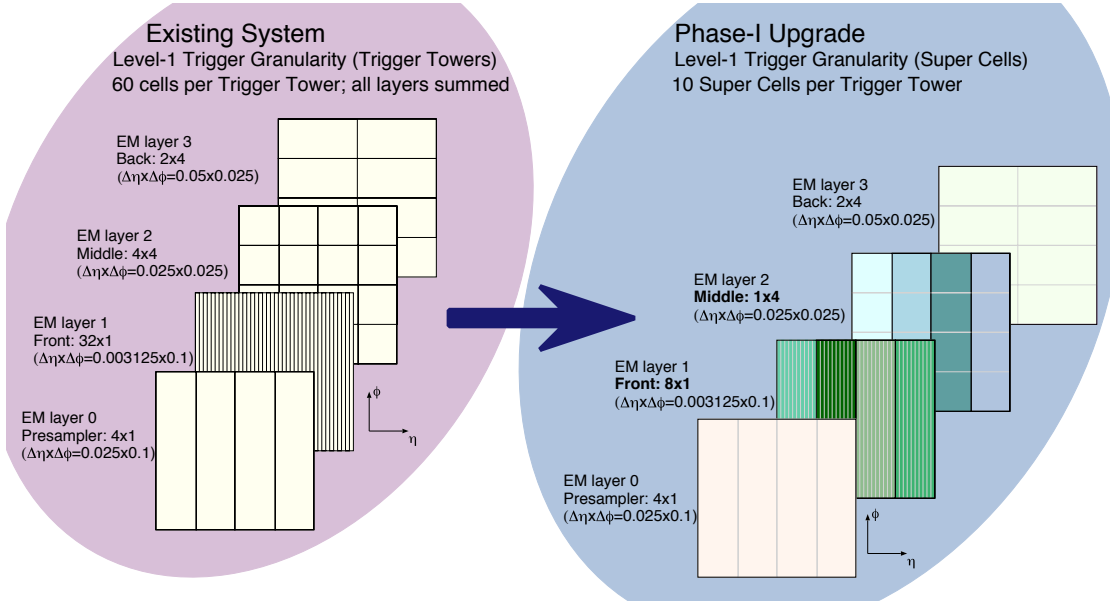


Figure 3.12.: Geometrical expansion in η , ϕ of a TT and the corresponding SCs in the EMB in the region of $\Delta\eta \times \Delta\phi = 0.1 \times 0.1$ [28]. For the current trigger readout system with TTs, all elementary cells within this region are summed over all the layers. For the future readout with SCs, different layers will be read out separately and the granularity in the front and middle layer is enhanced.

The identification of an SC in the EMB can be done with three parameters - the layer l , i_ϕ and i_η :

$$\begin{aligned} i_\phi &= \text{int} \left(\frac{\phi}{2\pi} \cdot 64 \right), \\ i_\eta &= \text{int} \left(\frac{\eta}{\Delta\eta(l)} \right), \end{aligned} \tag{3.6}$$

where $\Delta\eta(l)$ can be found in table 3.1. The table also shows the dimensions of the SCs in different layers, consisting of a certain number of elementary cells. In addition, the side of the detector must be considered, since the EMB consists of two symmetrical half-barrels, centered around the z-axis.

A recommended precise identification of an SC is the Supercell Identification (SC ID). It is a 32 bit number and includes information on i_ϕ , i_η , l , the detector side and other detector parameters like identifications of the different calorimeter parts. The identifications i_ϕ and i_η are preferred since ϕ and η include sagging effects which occur due to the influence of gravitation on the 7 000 tons detector. In detail the SC

3. The Experiment

Table 3.1.: Listing of the different granularities of TT, SC and elementary cell readout in the LAr EMB. Listed are the the dimensions in terms of elementary cells $n_\eta \times n_\phi$ and $\Delta\eta \times \Delta\phi$ (Data from [28]).

Layer		Elementary Cell	Trigger Tower		Super Cell	
		$\Delta\eta \times \Delta\phi$	$n_\eta \times n_\phi$	$\Delta\eta \times \Delta\phi$	$n_\eta \times n_\phi$	$\Delta\eta \times \Delta\phi$
0	Presampler	0.025×0.1	4×1		4×1	0.1×0.1
1	Front Layer	0.003125×0.1	32×1	0.1×0.1	8×1	0.025×0.1
2	Middle Layer	0.025×0.025	4×4		1×4	0.025×0.1
3	Back Layer	0.05×0.025	2×4		2×4	0.1×0.1

ID bits decode the identifiers listed in table 3.2. For more information on the readout identifiers see [40].

Figure 3.13 visualizes the difference in the readout of the former trigger system (figure 3.13(a)) and the future one (figure 3.13(b)) for the same event. The TT based readout detects a deposited transverse energy of 70 GeV in one TT. In contrast with that, the SC based readout provides the shape of the shower of the particle. Since electrons and jets have slight differences in their shower shapes, by quantifying these, it is possible to distinguish between them. The much finer granularity due to the finer quantization scale and additional informations in the calorimeter longitudinal layer makes it possible to achieve this by using SSVs.

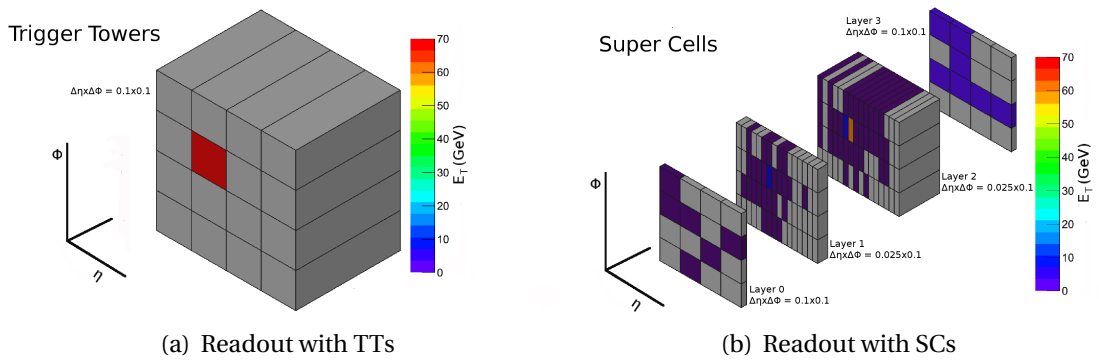


Figure 3.13.: 70 GeV electron shower in the LAr calorimeter read out by the TT based trigger readout (a) and by the SC based readout (b) [28]. Whereas in a) by reading out TT one can only learn the transverse energy, in b) we can see the shower shape of the particle.

Table 3.2.: Decoding of the SC ID bits. The definition of the detector readout identifiers is used in the ATLAS offline software [40].

Bits	23-31	21-22	15-20	9-14	1-8	0
Identifier	LAr Calorimeter LAr EM barrel	sampling (= l)	region	i_η	i_ϕ	side

3.4.3. Shower Shape Variables

As seen before in section 3.1.2, the instantaneous luminosity expected in Run 3 will be twice as high as the nominal luminosity. The trigger rates would increase to non acceptable values if the low- p_T thresholds, which are required by crucial physics studies, will be maintained. This is unless new discriminating criteria, like SSVs are introduced for the separation of electrons and photons from jets. Within this chapter a description on the three SSVs R_η , f_3 and $\omega_{\eta 2}$ is given.

The SSV R_η deals with the transverse extend of a shower. Since most energy of a shower is deposited in the middle layer, this layer is the object of interest. The transverse energy of an area of three times two SCs around the so-called hottest cell, where most energy was deposited, is summed up and divided by a more extended area of seven times two:

$$R_\eta = \frac{E_{T,\Delta\eta\times\Delta\phi=0.075\times0.2}}{E_{T,\Delta\eta\times\Delta\phi=0.175\times0.2}}. \quad (3.7)$$

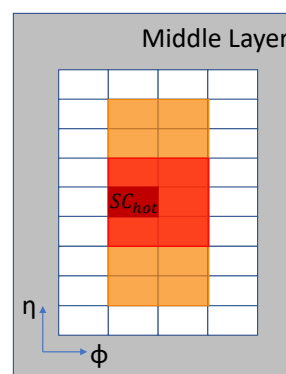


Figure 3.14.: Visualization of the R_η calculation.

Figure 3.14 visualizes the calculation. The first step is to identify the hottest SC in the middle layer. It builds the base of the summed areas. To decide, whether the two summed areas expand into $+\phi$ or $-\phi$ -direction, the two SCs next to the hottest SC in $\pm\phi$ -direction are examined. The SC, in which a higher energy deposition took place, determines the location of the summed SCs. In the example, the neighboured SC in $+\phi$ -direction was identified.

While electrons have a narrow shower shape, jets are spreading much more transversely (and also longitudinally). This is reflected in the peak-like distribution at $R_\eta = 1$ of the electrons, shown in figure 3.17(a).

3. The Experiment

Another shower shape variable is f_3 . It takes the longitudinal expansion of the shower into account. A region of two times two SCs around the hottest SC in the back layer is divided by the sum of the same region in the back layer, and an area of three times two SCs in the front and middle layer, which lie in front of the region in the back layer. The expansion of the summed areas in ϕ -direction is determined the same way as described above. The expansion in η -direction in the back layer is decided by the neighboured SCs in η -direction in the middle layer. See also figure 3.15.

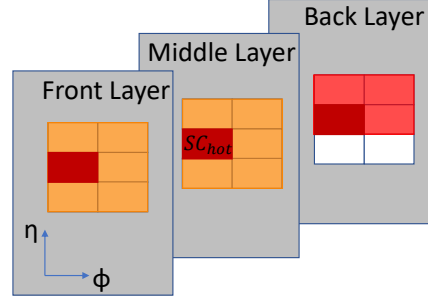


Figure 3.15.: Visualization of the f_3 calculation.

f_3 is calculated by

$$f_3 = \frac{E_{T,\Delta\eta\times\Delta\phi=0.2\times0.2}^{(3)}}{E_{T,\Delta\eta\times\Delta\phi=0.075\times0.2}^{(1)} + E_{T,\Delta\eta\times\Delta\phi=0.075\times0.2}^{(2)} + E_{T,\Delta\eta\times\Delta\phi=0.2\times0.2}^{(3)}}. \quad (3.8)$$

Due to their interaction mechanisms jets deposit more energy in the back layer compared to electrons. This is confirmed by the simulation in figure 3.17(b).

The third shower shape variable that is investigated is ω_{η^2} . It also takes into account the transverse shower expansion and represents a variance of the energy distribution in the middle layer (see figure 3.16).

An electron shower is more concentrated and defined than a jet shower. Therefore, the distribution for electrons is narrower than for jets. Additionally the mean value is smaller for electrons (see figure 3.17(c)).

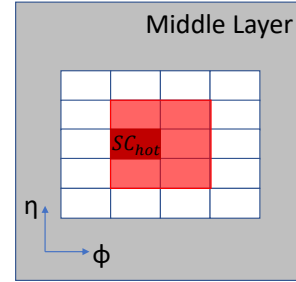


Figure 3.16.: Visualization of the ω_{η^2} calculation.

$$\omega_{\eta^2} = \sqrt{\frac{\sum (E_T^{(2)} \times \eta^2)_{\Delta\eta\times\Delta\phi=0.075\times0.2}}{E_{T,\Delta\eta\times\Delta\phi=0.075\times0.2}^{(2)}} - \left(\frac{\sum (E_T^{(2)} \times \eta)_{\Delta\eta\times\Delta\phi=0.075\times0.2}}{E_{T,\Delta\eta\times\Delta\phi=0.075\times0.2}^{(2)}} \right)^2} \quad (3.9)$$

3.4. Upgrade of the LAr Calorimeter Trigger System

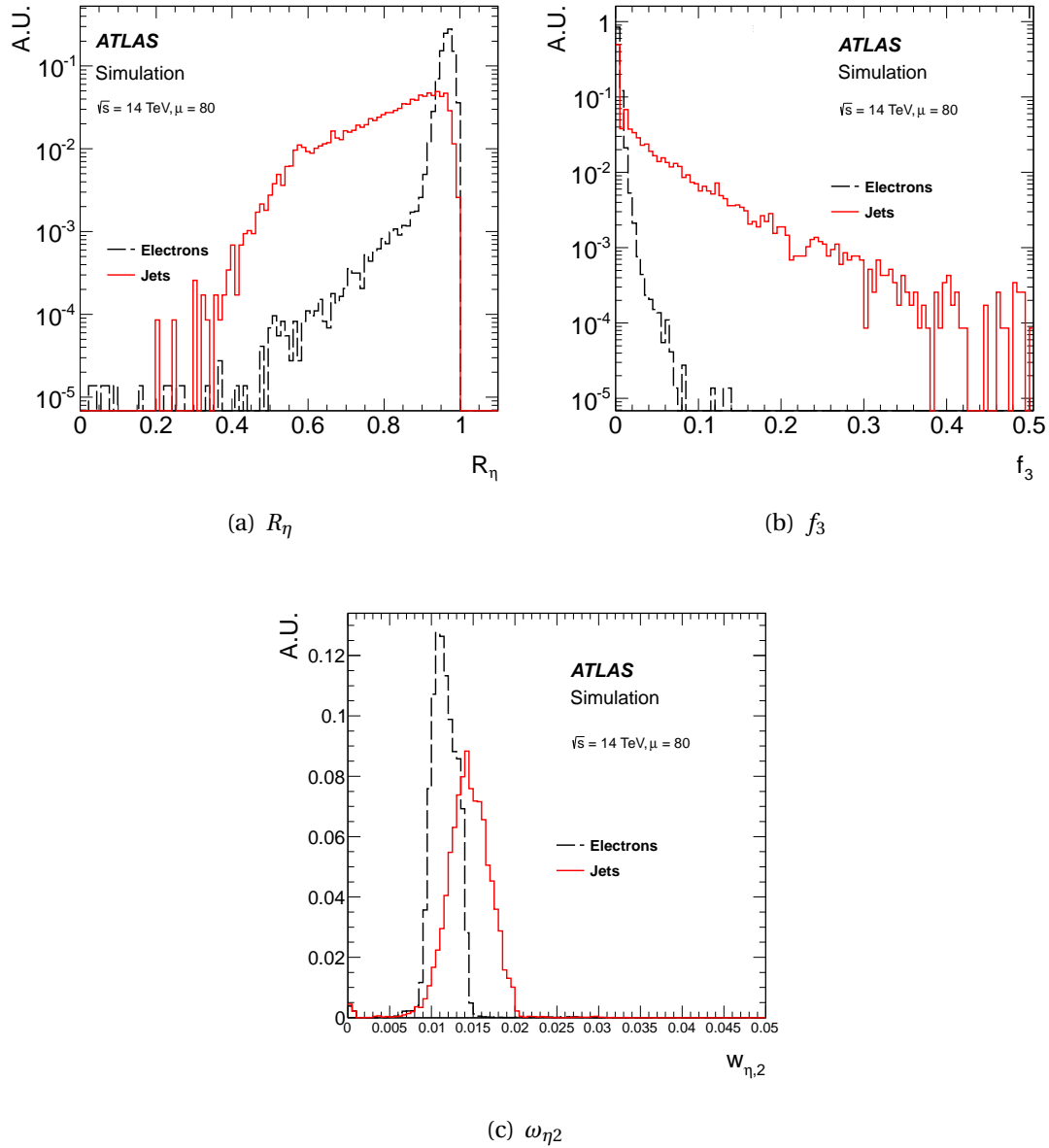


Figure 3.17.: Three different SSV that will be used for the calorimeter trigger [28].

3.4.4. The Demonstrator

In order to exercise the future higher granularity trigger readout of the ATLAS LAr calorimeters, a demonstrator system was installed during LS1. Figure 3.18 shows the region, where the demonstrator system takes data. It covers an area of $1.767 < \phi < 2.160, 0 < \eta < 1.4$ and includes a FEC which has been equipped with a non-radiation hard version of the electronics, that is foreseen for the Phase-1 upgrade [36].

The first aim was to validate that the demonstrator does not disturb or add noise to the current readout system. Another purpose was to gain experience on the SC pulse shapes and timing during Run 2.

The demonstrator setup consists of a front end part and a back end part. The front end electronics contains new LSBs, two backplanes and two LTDBs which are named after their place of manufacture, the Brookhaven National Laboratory (BNL) and the Laboratoire de l'accélérateur linéaire, Université Paris Saclay (LAL/Saclay). The LTDBs care for maintaining the old TT-based readout having at the same time the new Phase-1 readout system, operational based on SCs. From the LSBs, the SC signal is passed on to the LTDBs, where it is digitized with a granularity of 64 to 250 MeV (least significant bit) instead of 1 GeV for the analog version. The LTDBs process up to 320 SC signals. For the EMB these are 284 SCs. The digitization is done by 12 bit ADCs at 40 MHz [36].

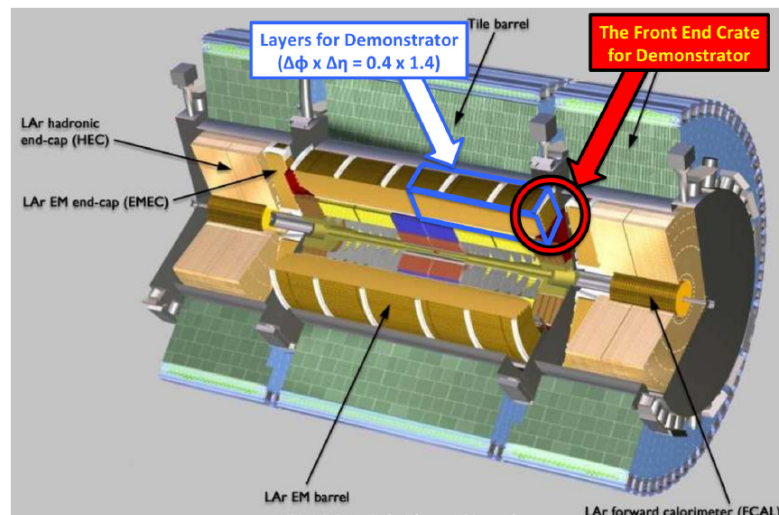


Figure 3.18.: Display of the readout region of the demonstrator setup [41].

3.4. Upgrade of the LAr Calorimeter Trigger System

The back end electronics contains a new LDPS which is called ATCA Board for a Baseline of liquid argon Acquisition (ABBA). At this point, data are read out and recorded if the demonstrator received a positive trigger signal. Four Field Programmable Gate Arrays (FPGAs) are located on the two ABBA boards, which read out SCs of the EMB of one specific i_ϕ . These are $i_\phi = 18, 19, 20, 21$. Since the Demonstrator cannot trigger itself, it is triggered for data readout. For this purpose two separate trigger items "L1-LAR-EM" and "L1-LAR-J" have been introduced to the trigger menu of the CTP. Whereas the former requires a L1 electromagnetic cluster with $E_T > 20 \text{ GeV}$, the second trigger item requires a L1 Jet with $E_T > 100 \text{ GeV}$.

More detailed information on the demonstrator system can be found in [42]. This thesis refers to the demonstrator system from 2017.

4. Analysed Data of the Demonstrator System and the ATLAS Main Readout

In order to assess the capability of the future high granularity SC readout for the L1 trigger system, data from the demonstrator readout were analysed. To compare the recorded information to expectation, data from the ATLAS main readout were used in addition. This section describes the datasets of these two different readouts. First, important data contents will be given for both readout systems. Moreover, the classification of the particle type of an event is explained as well as the calculation of the pulse peak sample and the energy reconstruction for the data of the demonstrator readout. Finally, problems occurring with the demonstrator data are described.

4.1. Data Samples

Much information about a triggered event can be obtained from the ATLAS main readout data, since it contain fully reconstructed events. For the demonstrator readout, no event reconstruction takes place. Instead, entries in the demonstrator dataset only contain raw data of sampled pulses, which were described in section 3.3.3, and need to be transformed into cell energies. The following sections describe the data used, their properties and content for the main readout and the demonstrator readout.

4.1.1. The ATLAS Main Readout

The datasets which were taken for the main readout are in Analysis Object Data format (AOD). These contain offline reconstructed information on events. This means that particle identification variables and kinematics are contained. They are created based on so-called Event Summary Data (ESD), which include detailed reconstruction of events and which are produced from raw data. A property of data in AOD format is

that it contains all necessary but reduced information on events. This decreases the file size compared to ESD, and makes it easier and faster to process data. However, this implies also, that there is reduced information on calorimeter cells. Only cells close to the hottest calorimeter cell, which received most energy of the particle, are contained [43].

As a first step, the datasets were converted into ROOT files and only the necessary information was extracted. Some of the important variables are listed below:

- **Run number:** During periods of data collection, the run number is the identification number of the recorded dataset.
- **BCID:** The Bunch Crossing Identification number is an integer between 0 and 3564. It identifies the crossing bunches in the LHC that caused the event. The assignment takes place at the L1 trigger. Since one bunch in the LHC crosses several times at the ATLAS detector during one run (at 11 kHz), this ID is not unique.
- **Level-1 Identification (L1ID):** This 32 bit number is divided into the Event Counter Reset Counter (ECRC) (first 8 bits) and the Event Counter (EC) (last 24 bits). With each L1A signal the event counter is increased. The ECRC is broadcasted by the TTC system and resets the EC.
- **Time stamp:** There are two different time stamp variables for an event. The first, often called "timeStamp" or "BCTime" marks the time in unix time, when the event took place. Since this is very imprecise, the second variable, which is called "timeStampNOffset" or "BCTimeNS", describes the event time offset to the last full second in nanoseconds.
- **Trigger Type (TType):** includes information on the trigger. For its components, see table 4.1.
- **SC Et:** includes the transverse energy in MeV of an SC.
- **SC E:** includes the energy in MeV of an SC.
- **SC ID:** is a 32 bit number and includes the position of the SC in the detector. See also section 3.4.2.
- **SC Eta:** is the η -coordinate of the SC.
- **SC Phi:** describes the ϕ -coordinate of the SC.
- **SC Sampling:** identifies the layer (0 - presampler, 1 - front layer, 2 - middle layer, 3 - back layer) of the SC.

- **Variables on reconstructed particles:** preliminary particle assignments with information on their kinematics and event coordinates.
- **Particle selection variables** for electron, muon and photon.

Since there is only information on calorimeter cell energies in the AOD datasets, the energy for an SC is calculated by summation of the corresponding calorimeter cell energies. As there is a cut on the information for the calorimeter cells, SCs that lie on the edges of an event might have underestimated energies. For minimizing the file sizes, only information on SCs that lie within the demonstrator readout region are available in the ROOT files. This includes SCs with $i_\phi = 18, 19, 20, 21$ and $i_\eta = [0, 55]$ for the front and middle layer and SCs with $i_\phi = 18, 19, 20, 21$ and $i_\eta = [0, 13]$ for the presampler and back layer.

The TType is an 8 bit number (see Table 4.1), which accompanies the L1A. Both are distributed via the TTC signal. The TType encodes the trigger decision. Its bits are based on several different L1 trigger items.

The first bits indicate, which subdetector caused the trigger to fire. "Random" and "ZeroBias" events are randomly triggered events based on different algorithms [44]. The "Calorimeter" bit states whether the energy deposit in the calorimeter has caused the trigger decision. When the 3rd bit is set, a muon was triggered at the corresponding event. The most important bit in the analysis is the LAr demonstrator bit as it indicates whether the demonstrator setup was triggered. The "FTK" bit is based on the Fast Tracker (FTK) [45]. The FTK is an electronics system, which reconstructs tracks after the L1 trigger decision. It gives early access to tracking information for the L2 trigger. For example the FTK contributes to the selection of processes like $H \rightarrow \tau\tau$. The "ALFA" bit arises from a sub-detector called Absolute Luminosity For ATLAS (ALFA) [46] that is located 240 m from the interaction point. Aim of this detector is to measure elastic pp-scattering and small angles in the Coulomb-Nuclear Interference (CNI) region. Bit 7 describes whether the ATLAS detector is running in physics mode, meaning that pp-collisions are recorded. In calibration mode it will be unset. In the analysis of the LAr demonstrator physics data it is thus at least required for bit 4 and 7 to be set.

Table 4.1.: 8 TType bits and their identification [42].

Sub-trigger bit	physics	ALFA	FTK	LAr demonstrator	Muons	Calorimeter	Zero Bias	Random
	7	6	5	4	3	2	1	0

4.1.2. The Demonstrator Readout

The demonstrator readout stores raw data files in binary format. These are automatically processed into ASCII and then ROOT files. The latter were used for data analysis of this thesis and further descriptions refer to them. In addition to various information on run and readout specific parameters, the following important variables are stored in these files:

- **BCID:** The Bunch Crossing Identification number is an integer between 0 and 3564. It identifies the crossing bunches in the LHC that caused the event. The assignment takes place at the L1 trigger. Since one bunch in the LHC crosses several times at the ATLAS detector during one run (at 11 kHz), this ID is not unique.
- **LIID:** This 32 bit number is divided into the ECRC (first 8 bits) and the EC (last 24 bits). With each L1A signal the event counter is increased. The ECRC is broadcasted by the TTC system and resets the EC.
- **Time stamp:** There are two different time stamp variables for an event. The first, often called "timeStamp" or "BCTime" marks the time in unix time, when the event took place. Since this is very imprecise, the second variable, which is called "timeStampNOffset" or "BCTimeNS", describes the event time offset to the last full second in nanoseconds.
- **TType:** includes information on the trigger. For its components, see table 4.1.
- **SC Et:** includes the transverse energy in MeV of an SC.
- **Source ID:** Identification of the ABBA FPGA board. Every FPGA board can be related to an i_ϕ slice of the demonstrator readout region (see table 4.2).
- **ADC:** A container with 50 ADC samples of the shaped calorimeter pulse for 160 SCs.

Table 4.2.: FPGA identification of the demonstrator.

i_ϕ	LTDB	ABBA FPGA	Source ID
18	BNL	19:2	0x410512
19	BNL	20:2	0x410511
20	LAL/Saclay	19:1	0x410521
21	LAL/Saclay	18:2	0x410522

A peculiarity of these ROOT files is that data of one event is not collected to one but four entries of the ROOT tree. These four entries do not have to be successive in the file. For that reason, identification of a single event is very important, in order to be able to collect all information. If all ABBAs worked properly, there would be four entries for every event since there are four FPGA boards on the two ABBAs. As mentioned, every FPGA reads out SCs in the EMB of one specific i_ϕ . Since not all the fibers and channels of the FPGAs are connected, these are up to 160 SCs. The identification of the SC in the detector is possible by a mapping of the channel number.

4.2. Classification of Particle Type

In the ATLAS main readout, the identification of e.g. an electron starts with a so-called sliding window algorithm, which finds electromagnetic clusters with an energy above a certain threshold. If a cluster is found, a track is searched that is pointing to it. If there is a good match of track and cluster, the cluster is considered as an electron. Otherwise it is recorded as a photon [47].

To ensure good particle identification, selection criteria are applied. For electrons three levels of identification with different rejection power exist [47]:

- **Loose** criteria contain different cuts on the detector acceptance and on leakage into the hadronic calorimeter. Also constraints on shower shapes in the middle layer are applied.
- **Medium** criteria include all loose cuts and additionally, deal with cuts on SSVs of the front layer, as well as cuts on the track quality.
- **Tight** criteria are the strictest criteria. They include all cuts of the medium level. Additionally they contain identification cuts, that test the energy and momentum agreement and criteria on the TRT signal.

For the purposes of this analysis a medium cut is applied on electron events. Similar levels also exist for muons and photons.

On top of the requirements of an identification level, more selection criteria, e.g. on calorimetric or track properties can be used. For this thesis, official criteria on track and calorimeter isolation were applied [48]. Track isolation includes variables which ensure that tracks lie within a cone of a certain radius ΔR and possess a certain transverse momentum p_T . Calorimeter isolation describes energy deposition in the calorimeter within a cone of radius ΔR and above a certain energy threshold [47, 49].

In order to suppress background from hadronic jets, electrons were selected which fulfill one of the two following isolation criteria. The first criterion comprises that the sum of transverse energy in a cone of $\Delta R < 0.2$, E_T^{cone} , calculated from topological cluster energies is required to be small:

$$E_T^{\text{cone}} < 0.06 p_T, \quad (4.1)$$

where p_T is the transverse momentum of the electron. The second criterion requires the sum of momenta of all tracks in the same cone $\Delta R < 0.2$, p_T^{cone} , to pass

$$p_T^{\text{cone}} < 0.06 p_T. \quad (4.2)$$

Photons were selected, whose transverse energy in a cone of $\Delta R < 0.4$, E_T^{cone} , calculated from topological cluster energies fulfills

$$E_T^{\text{cone}} < 0.022 p_T + 2.45 \text{ [GeV]}. \quad (4.3)$$

Muons also were selected by two different criteria. The first criterion requires the sum of the transverse energy in a cone of $\Delta R < 0.2$, E_T^{cone} , to fulfill

$$E_T^{\text{cone}} < 0.06 p_T, \quad (4.4)$$

the second criterion requires the sum of momenta of all tracks in a cone of $\Delta R < 0.3$, p_T^{cone} , to pass

$$p_T^{\text{cone}} < 0.06 p_T. \quad (4.5)$$

For more information see [50].

Jets were selected, which fulfill the anti- k_t clustering algorithm [51] with a distance parameter $R = 0.4$ to electromagnetic topological clusters.

4.3. Pulse Peak Sample of the Demonstrator Readout Super Cells

For energy calculation of the SCs and assigning a BCID to each sample it is essential to know the peak sample of each SC. The location of the peak within a sample sequence should be fixed. In case for the demonstrator, it should lie in the 22nd sample, given by the relative delay of the L1A signal to the start of the signal readout. From figure 4.1, it can be seen that this is not the case for every SC. For example for the BNL board at $i_\phi = 18$, some channels (80-160) have their peak at sample 20. For this reason, the

4.3. Pulse Peak Sample of the Demonstrator Readout Super Cells

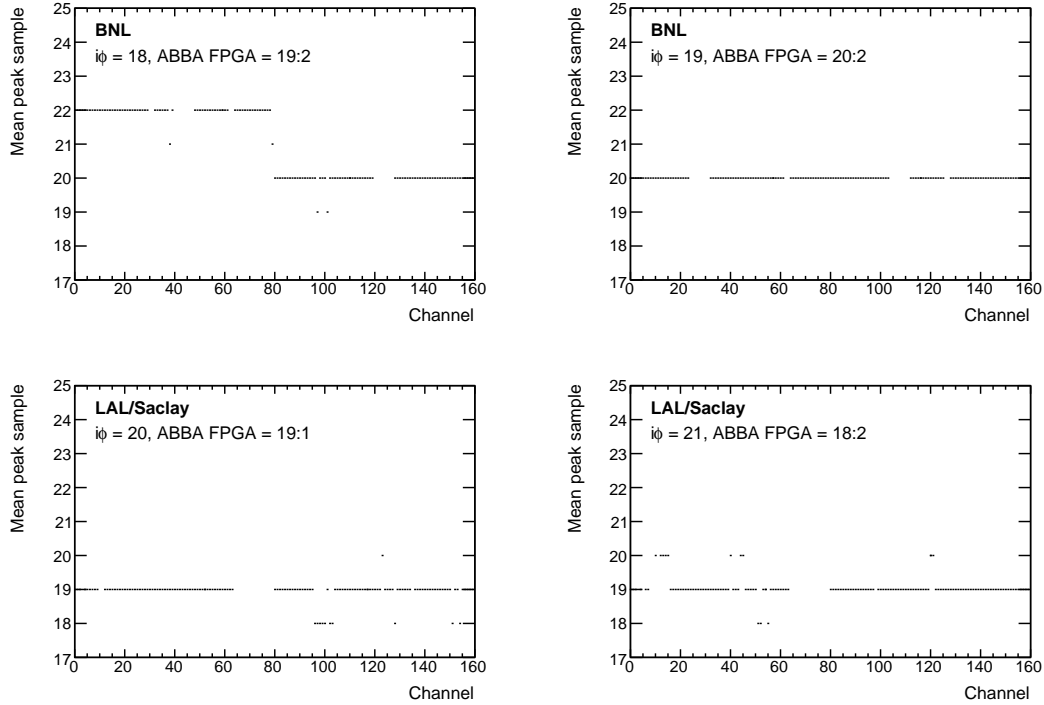


Figure 4.1.: Mean peak sample $S_{\text{reg}}^{\text{peak}}(SC_i)$ distribution for every channel of the two ABBA boards and their four FPGAs. Usually the peak position should be at sample 22. Due to system imprecisions this is not the case.

position of the peak sample was analysed for every SC_i and a map of the regular peak sample $S_{\text{reg}}^{\text{peak}}(SC_i)$ was created.

This analysis uses the event data described in section 4.1.2 (a list of the examined runs can be found in appendix A). First, all events with readout problems (which will be described in section 4.5) have been discarded and a threshold of $E_{\text{min}} = 4 \text{ GeV}$ was applied on the hottest SC. For these events, the hottest SC and eleven SCs that are positioned around the hottest SC have been analysed. These are the eight SCs in the middle layer that lie directly around the hottest SC and three SCs which have the same coordinates as the hottest SC in i_ϕ and i_η in presampler, front and back layer. For the purpose of simplification, it is assumed that these twelve SCs receive most energy of the particle, which deposits its energy in the EMB, compared to the other SCs within the layers. In reality, this does not have to be true, since particles might not fly straight through the detector layers.

For these twelve SCs the maximum sample has been taken to be the peak sample.

4. Analysed Data of the Demonstrator System and the ATLAS Main Readout

Processing all selected events gives enough information for statistical analysis for all SCs of the demonstrator readout region. Figure 4.2 shows distributions for two exemplary SCs of the middle layer. For both SCs, the distribution peaks at sample 22.

Nonetheless, samples 21 and 23 are considered as peak samples quite often as well. That shows that in the demonstrator readout, the location of the peak fluctuates, which leads to peak shifts beyond $S_{\text{reg}}^{\text{peak}}(SC_i)$. This will be fixed for the future system and is not the case for the ATLAS main readout. Because of these peak uncertainties, sample 22 is determined as the regular peak sample of these SCs, but a deviation of ± 1 has to be considered in all cases.

Figure 4.3 shows the same distributions for two SCs of the back layer. The right plot shows a clear peak at sample 22. For the left plot, interaction products of BCs before sample 10 have too large an impact on the distribution. In this case, the results for SCs of the same fiber are compared to estimate the most likely peak sample.

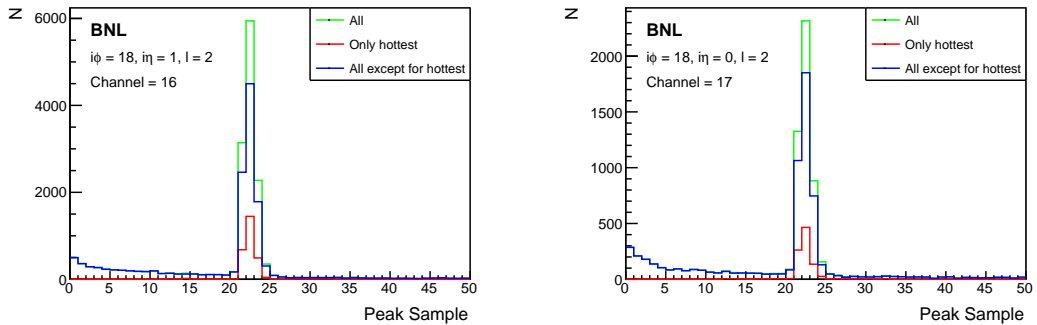


Figure 4.2.: Distributions of the peak sample of two different SCs in the middle layer for data from 2017. The red distribution takes events into account where the SC has been the hottest SC. The green distribution additionally takes all events into account, where the SC has been neighbored to the hottest SC. The blue distribution contains only events, where the SC has been neighbored to the hottest SC.

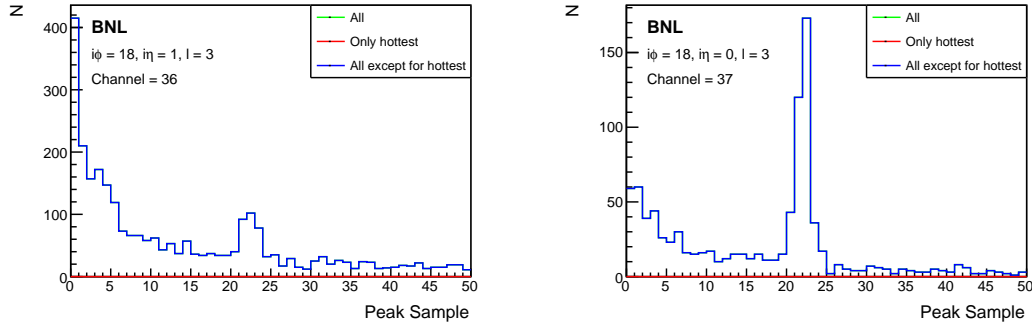


Figure 4.3.: Distributions of the peak sample of two different SCs in the back layer for data from 2017. The blue distribution contains events, where the SC has been neighbored to the hottest SC, which is the only possibility for compiling statistics for this layer.

4.4. Energy reconstruction of Demonstrator data

Since there is no internal energy reconstruction in the demonstrator readout, this has to be done directly on raw data.

As mentioned above, every digital signal of an SC_i in the readout region of the demonstrator is sampled by $N = 50$ samples s . Hence there are 50 ADC values $x(SC_i, s)$ which describe a pulse in an SC. The amplitude $A(SC_i)$ of a pulse is proportional to the energy $E(SC_i)$ deposited in an SC. For translating the amplitude into an energy, calibrated conversion factors, which are available for every SC, were used. The energy calculation is done in several steps. First, the calibrated pedestal value $p(SC_i)$ is subtracted from the ADC values and an Optimal Filter (OF) algorithm [52] is applied.

As a result, we get filtered ADC samples $x_{\text{OF}}(SC_i, s)$

$$x_{\text{OF}}(SC_i, s) = \sum_{i=0}^{M-1} a_i(SC_i) \cdot (x(SC_i, s - i) - p(SC_i)). \quad (4.6)$$

For visualization see figure 4.4. By using the OF with a depth of M and coefficients a_i , the amplitude and time of the peak of a pulse, which has been superimposed with electronic noise and pile-up, can be reconstructed. Since the OF is based on the calculation of a weighted sum over the relevant sample amplitudes, it needs at least M samples to work correctly.

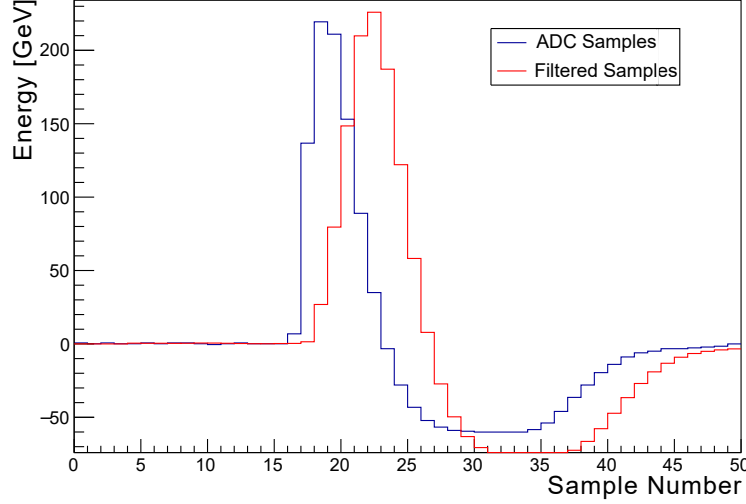


Figure 4.4.: Bipolar pulse of the demonstrator readout. Displayed are ADC samples (blue) and the response of the OF (red) [53]. For better comparison, both pulse distributions are displayed in energy units. For the ADC samples, the pedestal was subtracted and the result was converted into energy values by calibration factors. For the pulse with filtered samples, the ADC samples were subtracted by the pedestal, the OF algorithm was applied and the energy was reconstructed by calibration factors.

As a first step in peak reconstruction the maximum of all optimal filtered ADC samples was assigned to the signal amplitude. This approximation may overestimate the true energy especially in the presampler and front layer. The reason for this is that in these layers, only small amounts of energy are deposited and pile-up signals in the first samples can have higher ADC values than the actual signal. Therefore, the regular peak sample $S_{\text{reg}}^{\text{peak}}(SC_i)$ was used to give reference to the signal peak position. Due to the in section 4.3 mentioned peak uncertainties, the BC identified by the hottest cell SC_{hot} is defined as the peak sample position $S_{\text{irreg}}^{\text{peak}}(SC_{\text{hot}})$. It was assumed that within an event the peak shift of the hottest SC is the same for all SCs or at least similar. The deviation of these two values

$$\Delta S^{\text{peak}} = S_{\text{irreg}}^{\text{peak}}(SC_{\text{hot}}) - S_{\text{reg}}^{\text{peak}}(SC_{\text{hot}}) \quad (4.7)$$

is then added to all regular peak samples of cells in that event:

$$S^{\text{peak}}(SC_i) = S_{\text{reg}}^{\text{peak}}(SC_i) + \Delta S^{\text{peak}}. \quad (4.8)$$

The pulse amplitude of an SC is then calculated by finding the maximum of the filtered ADC values of this sample $S^{\text{peak}}(\text{SC}_i)$ and their two neighbouring samples

$$A(\text{SC}_i) = \max_{d=-2}^{+2} x_{OF}(S^{\text{peak}}(\text{SC}_i) + d). \quad (4.9)$$

The two neighbouring samples are also taken into account since the peak shifts might differ between cells in different layers.

To convert ADC values into an energy, calibrated conversion factors are applied next. They translate ADC values into an energy $c_E(\text{SC}_i)$ and include factors which correct the differences in high voltages $c_{HV}(\text{SC}_i)$:

$$E(\text{SC}_i) = c_{HV}(\text{SC}_i) \cdot c_E(\text{SC}_i) \cdot A(\text{SC}_i). \quad (4.10)$$

4.5. Issues with Demonstrator data

During data taking of the demonstrator system, different readout problems occurred. Figure 4.5 shows problems affecting the signal. Figure 4.5(a) and figure 4.5(b) show highly shifted peaks. If the peak sample $S_{\text{irreg}}^{\text{peak}}(\text{SC}_{\text{hot}})$ of the hottest SC is too much different from the regular peak sample $S_{\text{reg}}^{\text{peak}}(\text{SC}_{\text{hot}})$ of the SC, the rising edge or the undershoot of the signal pulse can disappear from the sampling window. In this case, the OF algorithm cannot reconstruct the pulse amplitude correctly. Therefore a restriction of

$$\Delta S^{\text{peak}} \leq 10 \quad (4.11)$$

was applied on the deviation of the peak sample of the hottest SC compared to the reference peak sample position $S_{\text{reg}}^{\text{peak}}(\text{SC}_i)$. Noise peaks may appear (figure 4.5(c)) with narrower pulse shapes than regular and are rejected from the analysis.

Differently to the effects described above, which occur to single events, SCs may show readout problems during the entire run.

For several runs taken in 2017, not all four FPGAs were active. This results in missing data for the whole i_ϕ slice of the corresponding FPGA board. Since at least three

4. Analysed Data of the Demonstrator System and the ATLAS Main Readout

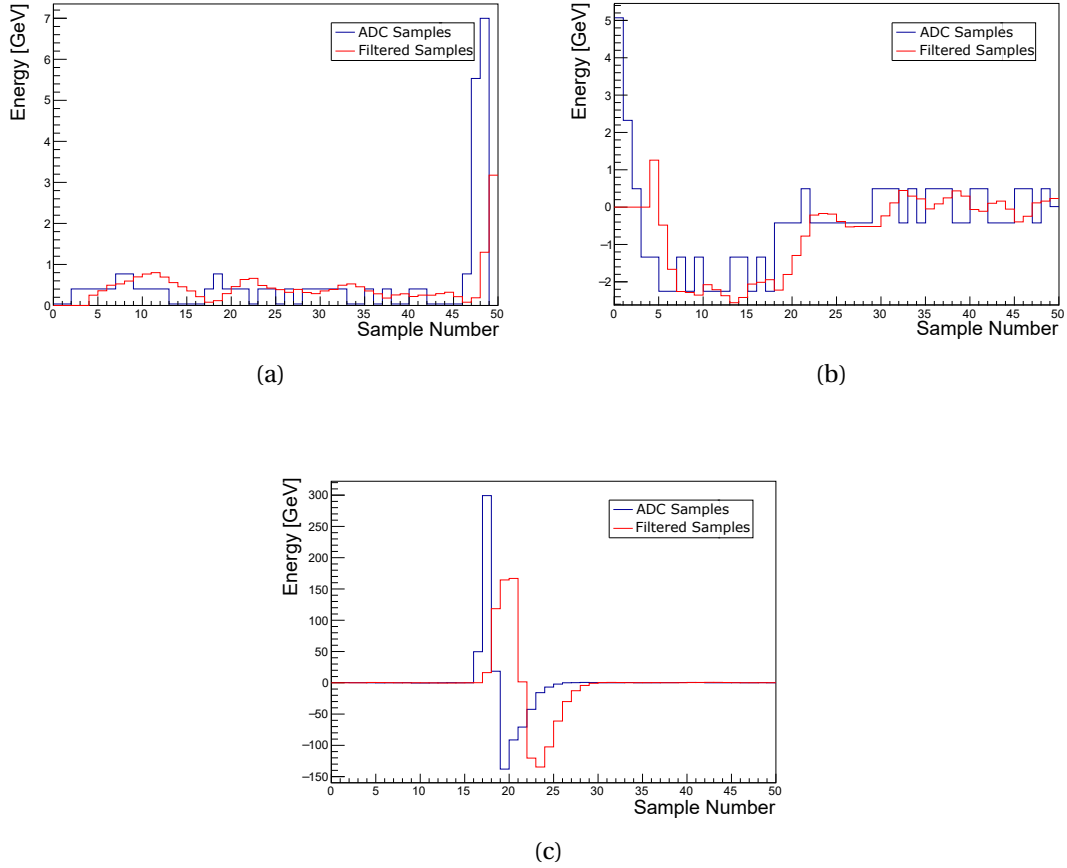


Figure 4.5.: Readout anomalies of the signal. Plots (a) and (b) show shifted pulses, whose energy reconstruction is not possible. In (c) a noise peak is displayed [53].

neighbouring cells in i_ϕ -direction are needed for calculating the SSV, this data could not be taken into account for the calculation of SSVs.

Figure 4.6 shows different patterns of SCs that needed to be excluded from analysis. Figure 4.6(a) shows the unlocked pattern from an SC. This cell was not connected and therefore delivers no information on the deposited energy. Plot 4.6(b) shows an SC that has a very high, abnormal pedestal. Usually, the pedestal should be at 1000 ADC counts ($\approx 1/4$ of the full range). Figure 4.6(c) shows jumping ADC counts without any regular pattern. Displays (d) and (e) of figure 4.6 show patterns of unstable pedestal values.

Reasons for the discovered anomalies are still unresolved to some extent. One likely

explanation is the lack of radiation hardness of the LTDBs of the demonstrator readout, which can cause bit flips and data corruption. This will be improved for the future readout system. For the analysis presented in this thesis, such SCs were excluded via a simple algorithm. Only SCs whose first five samples deviate from the calibrated pedestal value by no more than 10 % were included in further analysis.

4. Analysed Data of the Demonstrator System and the ATLAS Main Readout

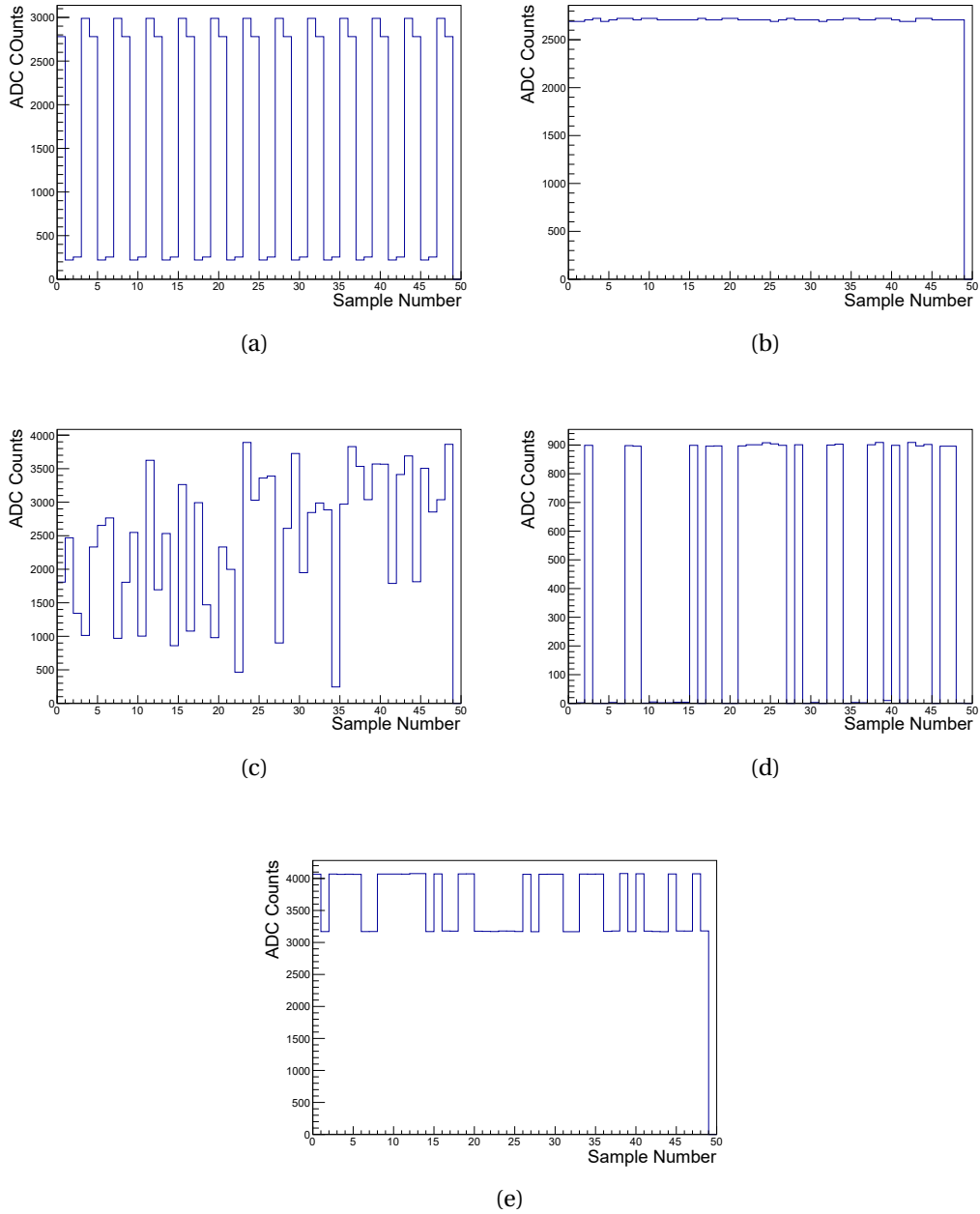


Figure 4.6.: Readout anomalies of the signal. Plot (a) shows the so-called unlocked pattern, which occurs for disconnected channels. Plot (b) shows a very high pedestal. Plots (c), (d) and (e) show SCs with strongly fluctuating ADC counts.

5. Comparison of Demonstrator and ATLAS Main Readout

In order to check the data quality of the demonstrator readout, information about an event recorded by the demonstrator system and its reconstructed energy was compared to the corresponding reconstructed event in the ATLAS main readout. This is the basis for further studies on SSVs. This chapter describes the matching of the events, the comparison of the reconstructed energies, and the comparison of the distributions of the SSVs for both readout systems. The SSVs R_η , f_3 and $\omega_{\eta 2}$ are examined for electron and jet events.

5.1. Matching of Data

To directly compare the two datasets, each event of a run from the demonstrator readout was matched to the corresponding event in the ATLAS main readout. Variables for the event identification like the BCID, L1ID and the time stamp are suitable for this purpose. Using L1ID and BCID gave a satisfying match of about 99% for each of the examined 85 runs. A list of the examined runs can be found in appendix A. Another variable which needs to match for both readout systems is the trigger type variable, because for one event, the trigger should have triggered both readout systems for the same reason.

About 3 million events have been successfully matched and processed. A fraction of 95 % could be used for analysis. This is due to the selection criterion $\Delta S^{\text{peak}} \leq 10$ that was introduced in section 4.5. Further events had to be excluded due to different readout problems of single SCs, which will be described later.

The decision whether an event was caused by an electron, jet, muon or photon is possible due to the information in the main readout data. By matching each event of the demonstrator readout and the main readout of the ATLAS detector, this information could be transferred to the event that was read out by the demonstrator system.

5. Comparison of Demonstrator and ATLAS Main Readout

As an example, figure 5.1 shows the energy of a particle deposited in all four layers of the EMB for the main readout and the demonstrator readout. Both readout systems show good agreement of the energy deposits in the same SCs. For the ATLAS main readout, a second region with energy deposition can be seen. It is not visible in the demonstrator readout because of a 4 GeV threshold that is applied to the hottest SC in the demonstrator data analysis.

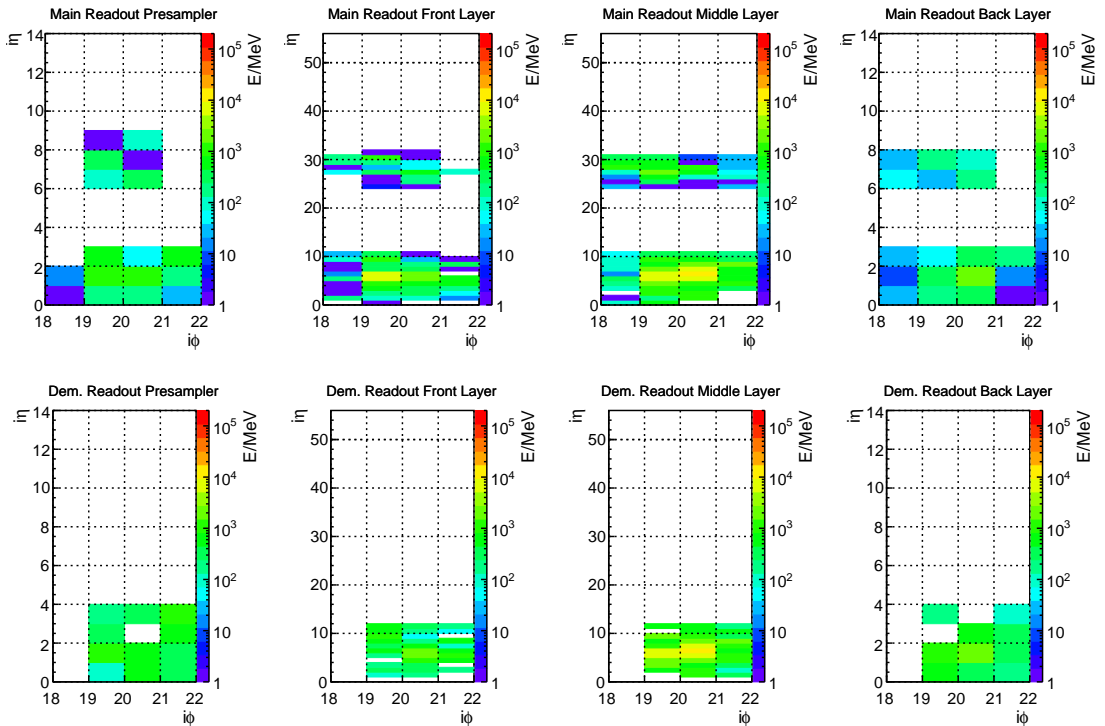


Figure 5.1.: Energy deposits in the EMB SCs of one event read out by the ATLAS main readout (upper) and the demonstrator readout (lower). Clearly visible is, that the most energy is recorded in the middle layer. Since the middle layer has the largest extent, most energy is deposited there and the hottest SC always lies within this layer. Because AOD data does not contain the full calorimeter information, not all SC energies can be shown. For the demonstrator, the SC energy is available for all SCs. Nonetheless, here it is displayed only for a region around the hottest SC.

5.2. Energy Correlation of the two Readout Systems

In figure 5.2, the correlation of the energy deposits in the SCs read out by the main ATLAS readout and by the demonstrator system is displayed. As explained in chapter 4, for the main readout SC energies are calculated by the summation of the corresponding calorimeter cells, whereas for the demonstrator readout, SC energies are based on SC signals. At event selection, a threshold of 4 GeV for the hottest SC in the middle layer for both readout systems was applied. Electron, photon, muon and jet events which were selected as described in section 4.2 contributed to the analysis.

Figure 5.2 shows that the correlation for all the four layers is satisfying. However,

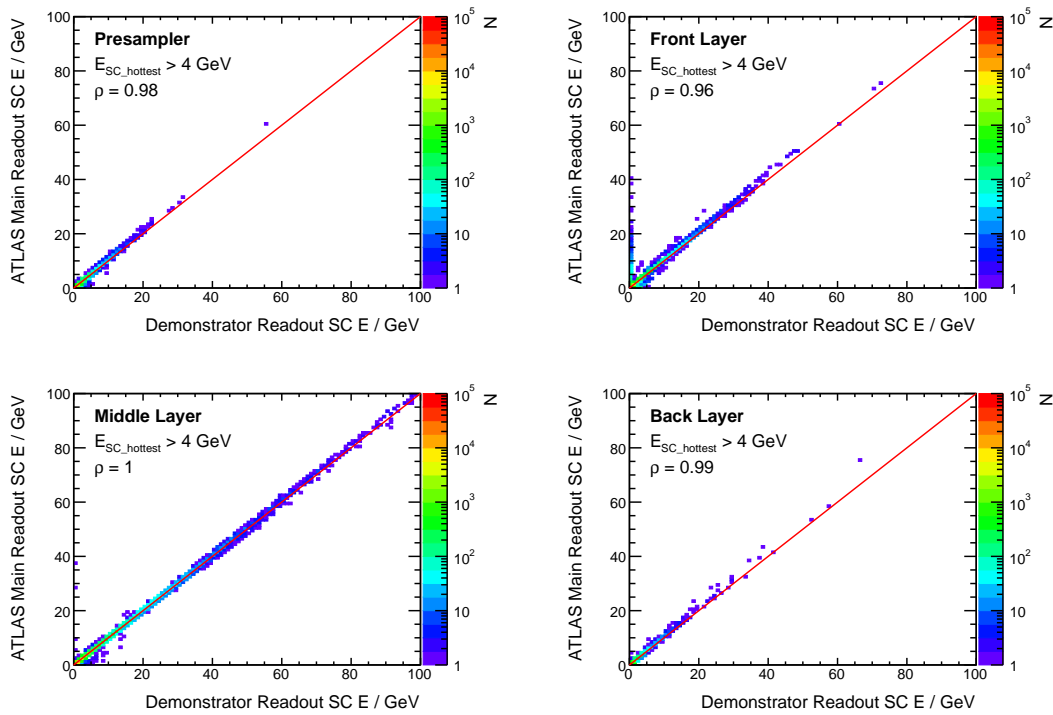


Figure 5.2.: Correlation of energy deposits in SCs of the ATLAS main readout and the demonstrator readout for each layer for run 330074. Only SCs in the middle layer lying directly beside the hottest SC in i_ϕ -direction and the two neighboured SCs in i_η -direction are considered. For presampler, front and back layer the SCs lying in front and behind this pattern were taken into account.

5. Comparison of Demonstrator and ATLAS Main Readout

especially in the front and middle layer, there are entries where the main readout shows non-zero energy entries, while for the demonstrator no energies were reconstructed (see also figure 5.3). During these events, the demonstrator readout measures only pedestal values for the corresponding SCs. Explanation can be found in already mentioned readout problems of the demonstrator where some cells show abnormal behaviour for unknown reasons. Since the LTDBs of the demonstrator are not radiation tolerant, this could be one explanation for the readout problems.

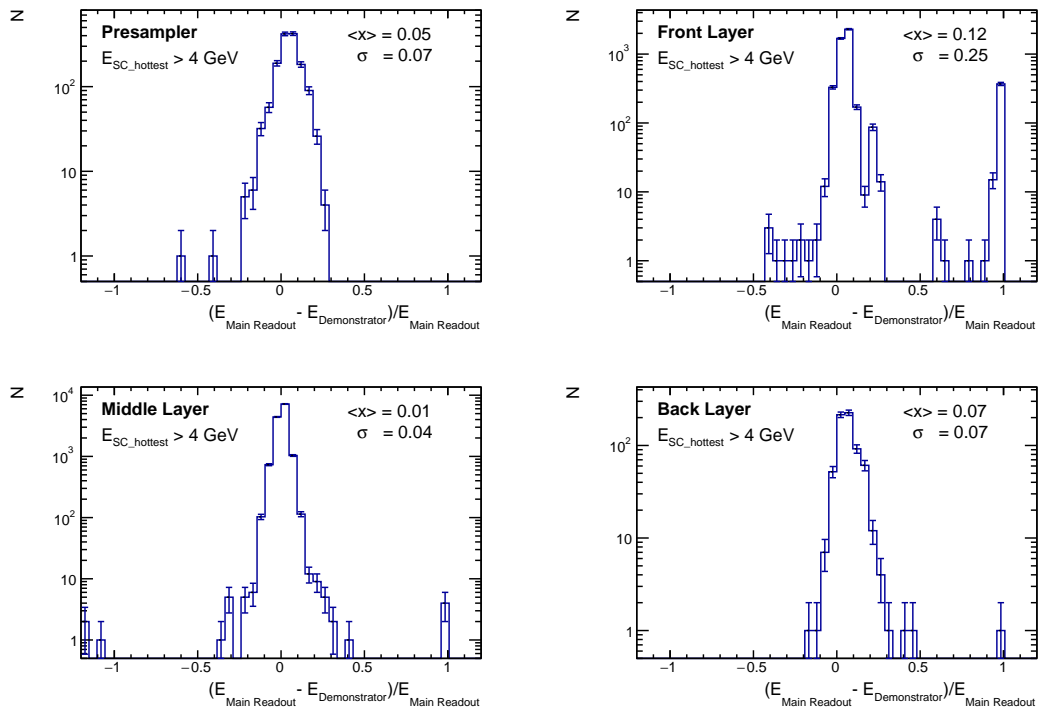


Figure 5.3.: Relative energy deviation in the energy reconstructed in the SCs for the ATLAS main readout and the demonstrator readout, separated by layer for run 330074. Only SCs in the middle layer lying directly beside the hottest SC in i_ϕ -direction and the two neighbouring SCs in i_η -direction are considered. For presampler, front and back layer, the SCs lying in front or behind this pattern were taken into account. Events in which the demonstrator system did not reconstruct any energy deposit in the SC can be clearly distinguished.

5.3. Analysis of the Shower Shape Variables

In the analysis of shower shapes, for the ATLAS main readout, about 2 000 electrons and 580 000 jets were taken into account in total. The discrepancy compared to the total number of 3 million analysed events has three reasons.

- The first reason is the energy threshold of $E_{\min} = 4$ GeV which was applied on the hottest SC for both readout systems.
- The second reason is the fact that an SSV can be calculated only if there is fully reconstructed information on the SCs lying around the hottest SC. Due to the restricted region that is read out by the demonstrator, this is not the case for events which have their hottest cell on the slices $i_\phi = 18$ and $i_\phi = 21$. The neighbouring cells are missing and so the calculation of e.g. R_η is not possible. If for example the hottest cell lies within $i_\phi = 18$, it is not possible to get information on the neighbored cells in $i_\phi = 17$ for data from the demonstrator readout. If there was more energy deposited on the slice $i_\phi = 17$, by taking the only-existing slice $i_\phi = 19$, R_η will be estimated incorrectly. Therefore only events with their hottest cell in $i_\phi = 19$ or $i_\phi = 20$ can be used. The same applies to the position of the hottest cell in i_η -direction. It must lie within $2 < i_\eta < 53$.
- The last reason is that only electrons and jets were considered for this analysis, whereas the numbers given in section 5.1 also included muon and photon events.

After removing data with readout problems or faulty SCs, about 1 100 electron and 310 000 jet events could be used for the shower shape analysis of the demonstrator readout.

5.3.1. R_η - Transverse Energy Ratio

Figure 5.4 shows the distribution of the SSV R_η for electrons and jets from the ATLAS main readout and the demonstrator readout. The distributions of electrons and jets are nicely separated, for both readout systems. The results show good qualitative agreement with the simulation shown in section 3.4.3.

As mentioned above for the ATLAS main readout, SCs that lie on the edge of a shower have underestimated energies. This will cause an overestimation of R_η , as the denominator in the equation is underestimated. Further reasons for discrepancies in the R_η -distributions of the different readout systems are the different digitization

5. Comparison of Demonstrator and ATLAS Main Readout

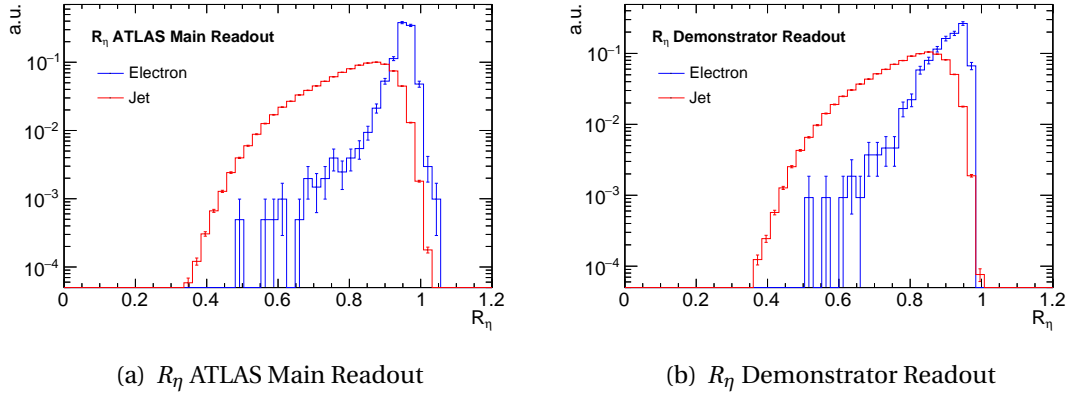


Figure 5.4.: SSV R_η for (a) the ATLAS main readout and (b) the demonstrator readout. Comparing the different readout systems, especially the distribution for jets is nearly the same. The distributions are normalized to 1.

scheme and energy reconstruction. For the main readout, SC energies are reconstructed by summing up the energies of the corresponding calorimeter cells which have a finer energy digital resolution of 16 bit than for the demonstrator readout SCs of 12 bit. SC energies of the demonstrator readout are reconstructed on the basis of SC pulses, using less validated correction factors than it is the case for the main readout of ATLAS.

5.3.2. f_3 - Shower Depth Variable

Figure 5.5 shows the distribution of the SSV f_3 . Generally, for the shape it shows agreement with the simulation, especially for jets. For both readout systems, the distribution for the electrons is wider than in the simulation.

SCs of the back layer in the demonstrator readout are much more susceptible to noise, and misreconstructed energies are more likely. This is because the energy of a particle deposited in this layer is comparatively small and due to peak shifts, fixing the pulse peak sample for calculating the signal amplitude is not possible as far as $S^{\text{peak}}(\text{SC}_i) \pm 2$ (see equation 4.9). Therefore, at the calculation of the signal amplitude, the actual pulse peak might be reconstructed incorrectly. Another reason for differences of figure 5.5(a) and figure 5.5(b) must be seen in the different digitization and the values of the LSB. Digitization effects become also visible in the small peaks at larger values of f_3 for both systems.

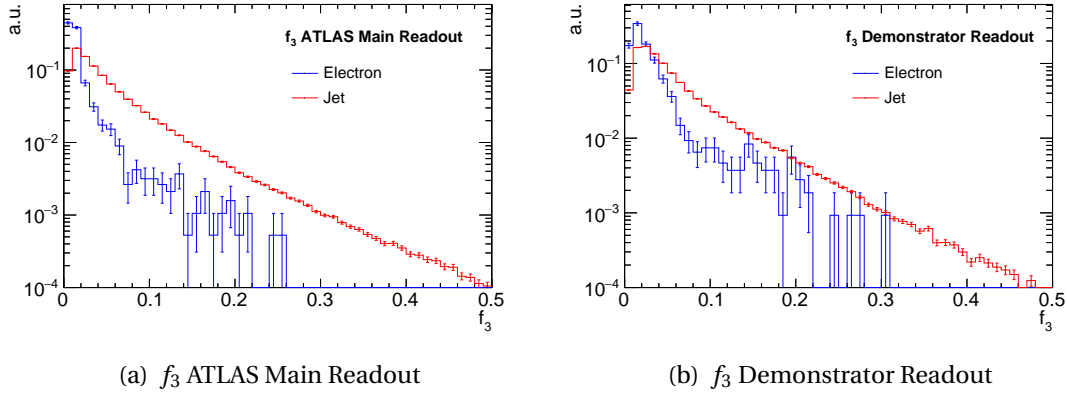


Figure 5.5.: SSV f_3 for (a) the ATLAS main readout and (b) the demonstrator readout. The distributions are normalized to 1.

5.3.3. $\omega_{\eta 2}$ - Shower Width

The SSV $\omega_{\eta 2}$ also shows good qualitative agreement with the simulation for both readout systems. In between the systems there are only minor differences in the distributions. Electrons and jets can be distinguished very clearly.

The improved particle distinction will make a great improvement for the future L1 trigger system, compared to the readout via TTs. An application of thresholds on the

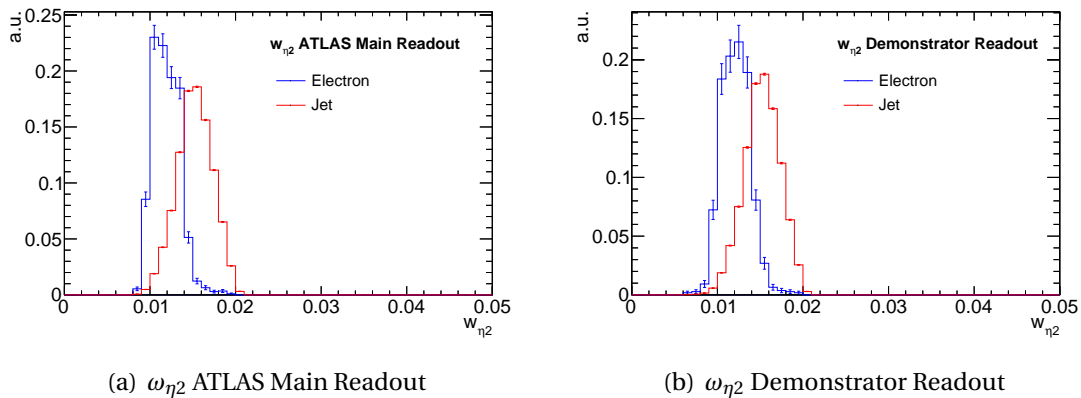


Figure 5.6.: SSV $\omega_{\eta 2}$ for (a) the ATLAS main readout and (b) the demonstrator readout. The distributions are normalized to unit area.

SSVs is foreseen, in order to select the more interesting events with electrons in the final state.

5.3.4. Correlation of the Shower Shape Variables

For the correlation of the SSVs in figure 5.7, only events were taken into account for which the demonstrator data could provide the calculation of the SSV. Also a cut of $E_{\text{SC}_{\text{hot}}} > 10 \text{ GeV}$ was applied.

The correlation of jet as well as of electron events show a considerable spread. Reasons for these discrepancies were already mentioned: Due to the main readout datasets used, the energies of SCs that do not lie directly next to the hottest SC are underestimated. Also, the different digitization scheme and energy reconstruction of the readout systems cause discrepancies. The discrete energy steps of the digitization has larger effects when energy ratios are calculated within the SSVs.

5.3. Analysis of the Shower Shape Variables

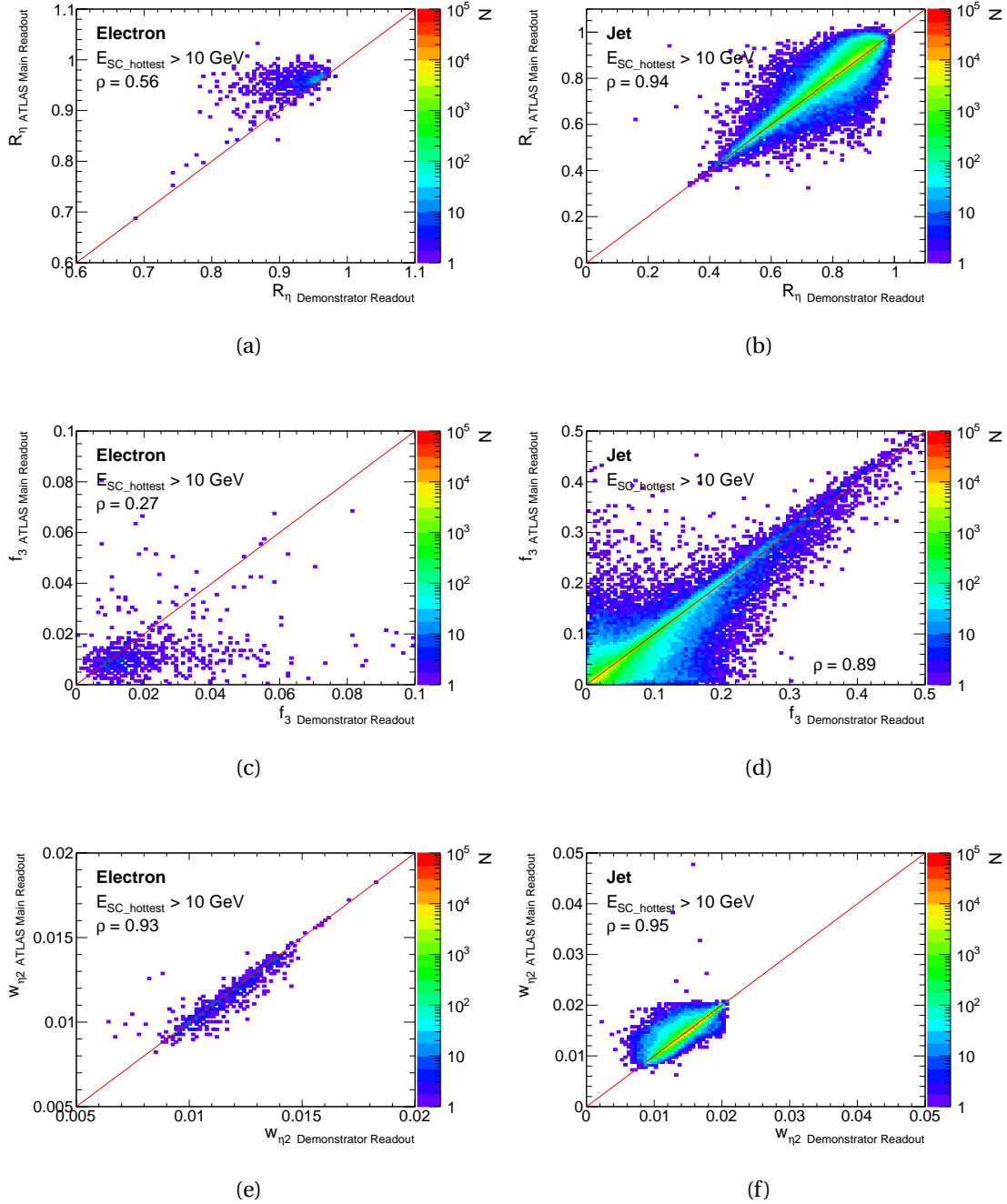


Figure 5.7.: Correlation of the SSV of the main readout of ATLAS and the demonstrator readout.

6. Pile-up Studies for the Demonstrator System

During Run 1, the average number of pile-up events per BC was $\langle\mu\rangle \sim 20$ at a peak luminosity of $\sim 7 \times 10^{33} \text{ cm}^{-2}\text{s}^{-1}$ and a center-of-mass energy of 8 TeV. In 2017, at a peak luminosity of $\sim 2 \times 10^{34} \text{ cm}^{-2}\text{s}^{-1}$ and a center-of-mass energy of 13 TeV, the mean pile-up increased to $\langle\mu\rangle \sim 55$ [36]. Therefore, it is important for future improvements to the data acquisition process, to investigate pile-up in order to figure out its impact on physics measurements. This chapter describes studies on pile-up based on data of the demonstrator readout. The mean pile-up energy per BC, the correlation of mean pile-up energy and luminosity as well as the single pile-up event energy spectrum will be presented.

Because the LHC BC frequency and the calorimeter pulse sampling frequency are the same, every ADC value of a sampled pulse can be assigned to a certain BC. The assignment uses the position of the peak sample, which corresponds to the event BCID.

As described in chapter 4, demonstrator data do not only provide information on single SC energies, but on whole SC pulses and beyond. Hence, it is possible to examine BCs that occur before or after the actual event that has been triggered. Because of the peak maximum being approximately at sample 22, the very first samples are unlikely to be affected by the signal pulse. Concerning SCs described in section 4.3, which do have their peak position at samples lower than 22, the samples 0 to 13 were regarded as not containing any signal but only pile-up energy deposition. Due to filter latency, the number of available samples decreases by four after the OF stage. This is due to the design of the OF, which in this case needs $M = 5$ (filter depth) samples to calculate one filtered sample. Therefore, only the ADC samples 2 to 11 can be taken into account. Figure 6.1 gives an idea of this issue.

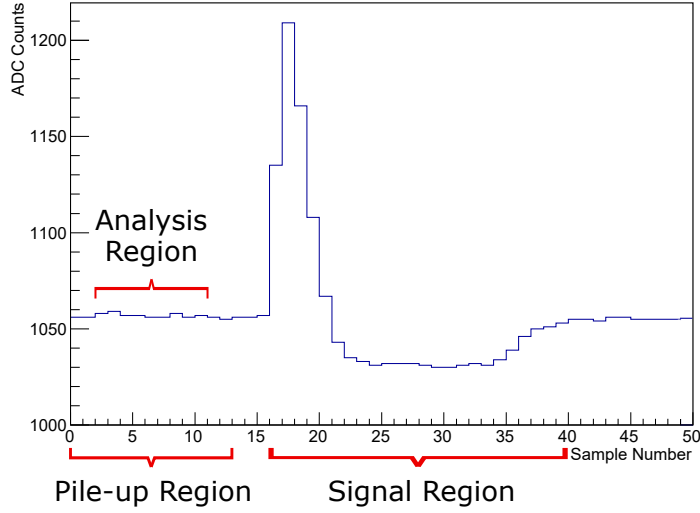


Figure 6.1.: Visualization of the pile-up and signal region.

6.1. Mean Pile-up Energy per Layer

In order to calculate the mean pile-up energy per BC, an event of a run that was read out by the demonstrator system was analysed as follows. The BCID of a chosen event $BCID_{\text{event}}$ corresponds to the peak sample $S_{\text{irreg}}^{\text{peak}}(SC_{\text{hot}})$ of the hottest SC pulse:

$$BCID(S_{\text{irreg}}^{\text{peak}}(SC_{\text{hot}})) \equiv BCID_{\text{event}}. \quad (6.1)$$

Using equation 4.7, the BCIDs of different samples s can be calculated as:

$$\begin{aligned} BCID(SC_{\text{hot}}, s) &= BCID_{\text{event}} - S_{\text{irreg}}^{\text{peak}}(SC_{\text{hot}}) + s \\ &= BCID_{\text{event}} - (S_{\text{reg}}^{\text{peak}}(SC_{\text{hot}}) + \Delta S^{\text{peak}}) + s. \end{aligned} \quad (6.2)$$

Since the peak sample of the hottest SC $S_{\text{irreg}}^{\text{peak}}(SC_{\text{hot}})$ is not necessarily the same for all SCs, it is necessary to take into account the corresponding SC peak samples $S_{\text{reg}}^{\text{peak}}(SC_i)$ and the peak shift ΔS^{peak} . Data for the regular SC peak samples were accumulated

as described in section 4.3. Thus, for every SC_i every sample s of the pulse can be allocated with its corresponding $BCID(SC_i, s)$ by:

$$\begin{aligned} BCID(SC_i, s) &= BCID_{\text{event}} - (S_{\text{reg}}^{\text{peak}}(SC_i) + \Delta S^{\text{peak}}) + s \\ &= BCID_{\text{event}} - S^{\text{peak}}(SC_i) + s. \end{aligned} \quad (6.3)$$

In the last step, equation 4.8 was used.

However, one has to be aware of the fact, that the peak shifts might differ between cells in different layers. Therefore, there is some uncertainty in the BCID of the pulse peak and the described calculation has some uncertainty for assigning the correct BCIDs to the samples.

Next, by using equation 4.10 the energy of each sample is calculated:

$$E(SC_i, s) = c_{\text{HV}}(SC_i) \cdot c_{\text{E}}(SC_i) \cdot x_{\text{OF}}(SC_i, s) \quad (6.4)$$

and separated by layer and BCID. After processing all events in this manner, the mean value over all events and SCs in a layer is computed.

Figure 6.2 shows the effect of pile-up within a bunch train. At the beginning, the signal amplitudes of the first occurring pile-up events accumulate and result in a peak of the mean pile-up energy deposition in the calorimeter. Pile-up events that take place from the middle to the end of a bunch train get affected by the undershoot of previous pile-up pulses. The undershoot of these and the peak of the pulse of the actual pile-up events cancel and the mean pile-up energy is zero by construction. In between two bunch trains the mean pile-up energy becomes negative. At these BCs, pulse undershoots lead to a negative overcompensation because no new pulses are caused in the detector.

In figure 6.3 the mean pile-up per BC for BCIDs within position 1950 and 2100 in the LHC orbit is displayed. At the beginning of the first bunch train, a peak is visible. From the middle to the end of the bunch train the mean energy becomes approximately zero. As expected, right in between the first and second bunch train one can see a negative mean pile-up energy. In the bunch train which begins at BC 2033, a peak which is lower than in the previous bunch train occurs. This is because the undershoot from the last pile-up events of the previous bunch train still have an impact on the mean energy. Therefore, this peak is comparatively smaller. Mean pile-up distributions for two exemplary SCs are provided in appendix B.

In figure 6.3 the rise and the fall of the pile-up distributions do not precisely match the beginning and end of the bunch train. This is due to the peak shifts for SC pulses

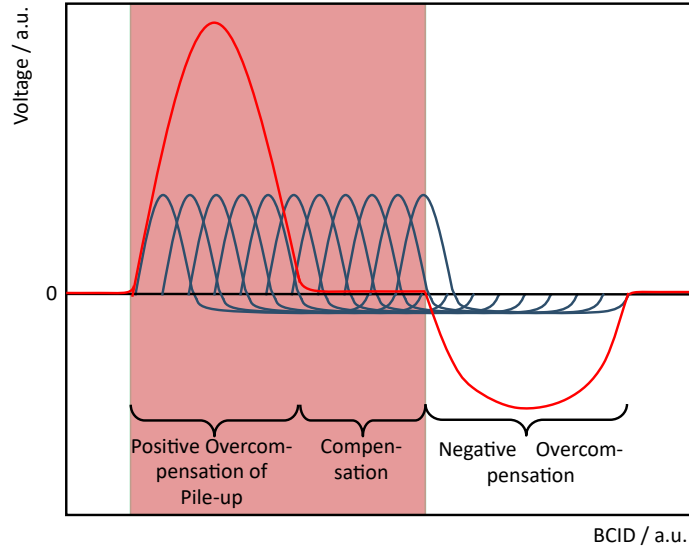


Figure 6.2.: Visualization of the positive and negative overcompensation of pile-up at the beginning and end of a bunch train. The highlighted regions in red show filled bunches, also known as bunch trains. The signal (red), which results from the superposition of single pile-up events (blue) is shown.

within the demonstrator readout. The cause of the negative mean pile-up energies occurring before the first bunch train, could not be verified, due to the limited scope of this thesis, but it is assumed that due to the averaging over SCs, it is originated by particular SCs.

Even though SCs in the presampler and the back layer have the same size, they do not receive the same amount of energy from pile-up events (see figure 6.3). This is because pile-up events do only have small energies compared to signal events and therefore most energy is deposited in the presampler. Low energy pions, which cause most pile-up, are absorbed in the first calorimeter layers already. The SCs in the front and the middle layer have the same dimension in ϕ and η direction but not for the \vec{r} direction. Here, the middle layer extends wider. Consequently, more energy is deposited in the middle layer than in the front layer.

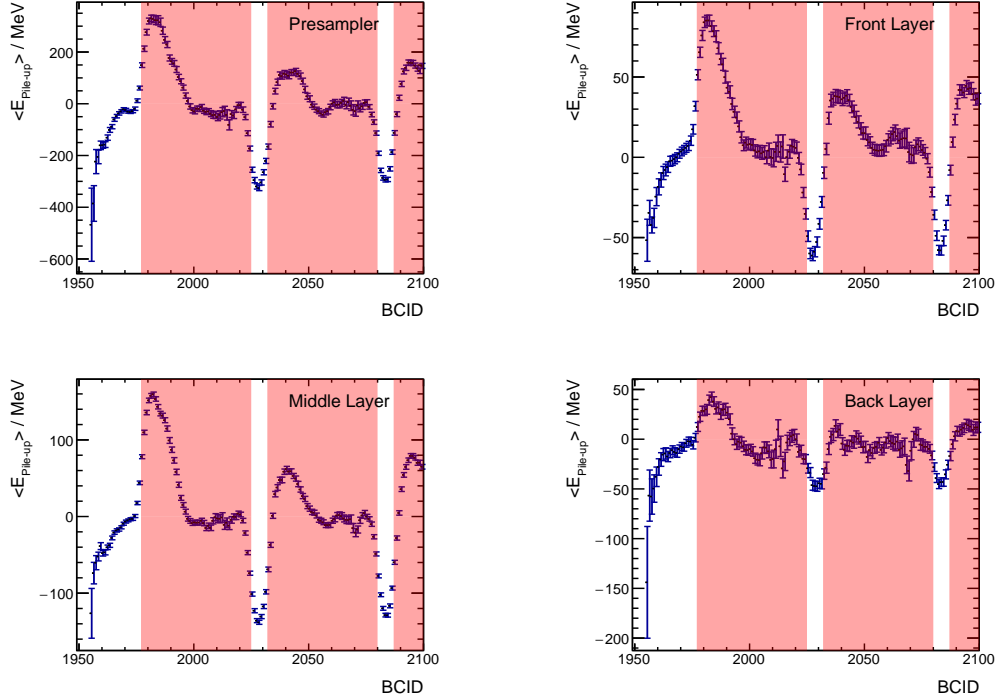


Figure 6.3.: Mean energy deposit of all pile-up events per BC separated by layer for run 332896. Only BCIDs within position 1950 and 2100 in the LHC orbit are displayed. Three bunch trains are highlighted in red.

6.2. Pile-up Time Spectrum

Figure 6.4 shows the mean pile-up energy plotted against the run time. The figures also show the time-dependent instantaneous luminosity.

For the mean energy, only samples with BCIDs fulfilling certain criteria have been taken into account. As seen in section 6.1, pile-up energy deposition is only visible within the first BCs of a bunch train. Hence, only those sample energies were considered whose BCID is the 5th after the beginning of a bunch train, which has at least 25 empty bunches beforehand. The 5th BC is used because of the OF's latency.

A correlation can be seen between the instantaneous luminosity and the distributions of the presampler, front and middle layer. Figure 6.5 displays the correlations $\rho(\langle \mathcal{L} \rangle_t, \langle E \rangle_t)$ for each layer. Because of the low energy deposits and low statistics, it is difficult to verify a correlation for the back layer. The small dips in the instantaneous luminosity in figure 6.4 are due to readjustments of the beam. The luminosity

6. Pile-up Studies for the Demonstrator System

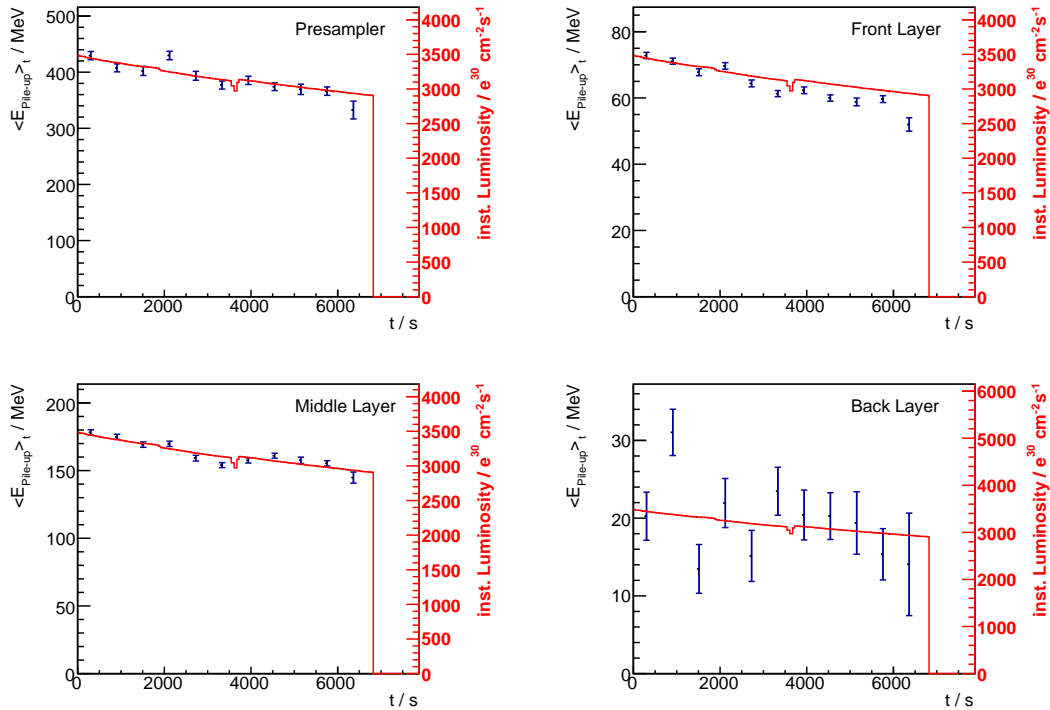


Figure 6.4.: Mean pile-up energy over time (blue) for run 332896. A correlation with the instantaneous luminosity (red) is visible.

decreases since the beam is filled with protons only at the beginning of a run. Due to the collisions, the number of protons decreases and so does the instantaneous luminosity. The difference in the mean pile-up energy between different layers is explained in the previous section.

6.3. Pile-up Energy Spectrum

For the pile-up energy spectrum analysis the same data as for the time spectrum in the previous section was used. Only sample energies, whose BCID is the 5th after the beginning of a bunch train, are taken into account. Additionally the bunch train has to have at least 25 empty bunches beforehand. As seen in section 6.1 only BCIDs with these criteria show pile-up energies that are not affected by pulse undershoots. Furthermore, a "maximum finder" algorithm was applied, which ensures that a sample energy only contributes to the spectrum, when the previous and the subsequent

6.3. Pile-up Energy Spectrum

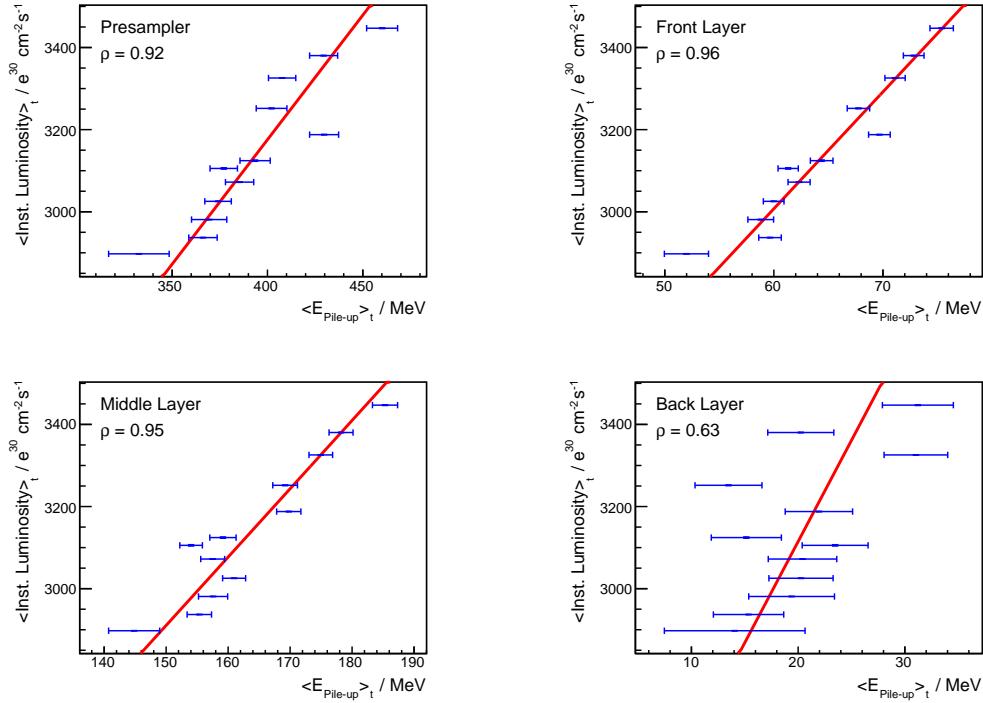


Figure 6.5.: Correlation of the mean instantaneous luminosity and the mean pile-up energy for each layer for run 332896.

sample energy is lower. The pile-up energy deposits were divided by the expected number of pile-up collisions μ , which correlates with the instantaneous luminosity.

Figure 6.6 displays the resulting distribution. Negative energies contribute to the distribution when the energy deposit of all pile-up events in a BC is smaller than the calibrated pedestal value.

Considering that the energy resolution in the calorimeter scales with $1/\sqrt{E}$ [4], pile-up at low energies is smeared. Therefore, the main peak for each layer in figure 6.6 is not as sharp as expected [54]. Deconvolution of the underlying energy resolution could be subject of further investigations in order to get a more precise pile-up energy spectrum. This is fundamental to calculate a pile-up correction. However, such investigations are beyond the scope of this thesis.

6. Pile-up Studies for the Demonstrator System

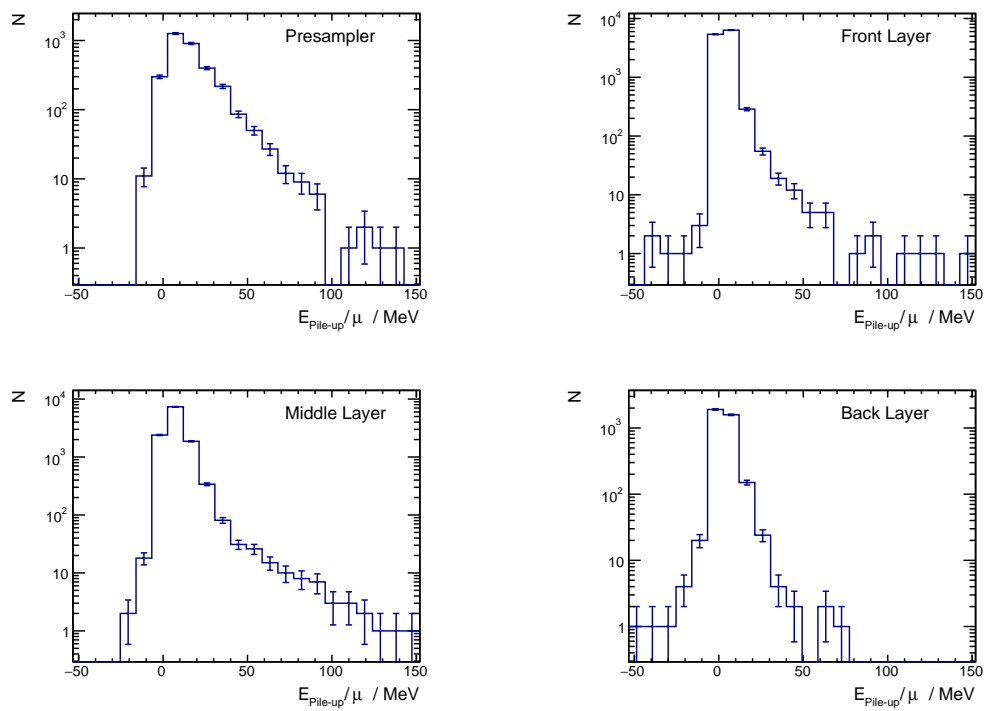


Figure 6.6.: Pile-up energy spectrum for each layer of run 332896. The spectrum is that of a single pile-up event.

7. Summary and Outlook

In order to be able to investigate rare physics processes it is desirable to increase the instantaneous luminosity of the LHC. This makes it necessary to improve the trigger system of the ATLAS detector. For improving the Level-1 trigger, a new calorimeter readout is foreseen, which reads out super cells instead of trigger towers and increases the calorimeter readout segmentation by a factor of 10. The higher granularity readout provides information on the shower shape of a particle in longitudinal and transverse direction. Thus, this will make it possible to quantify the shower shape at the first trigger level, already. For this thesis data that were recorded by the demonstrator system, which simulates the future trigger readout, were analysed. For comparison, data from the ATLAS main readout were matched to the data from the demonstrator readout and also analysed.

In the first part of this thesis, the data used, their properties and issues were explained. Withal the energy reconstruction for the demonstrator readout was described. Furthermore, challenges in the demonstrator data were discussed and described, how they were treated. Thereby, for some events super cells had to be excluded from the analysis but sometimes also whole files had to be discarded.

The second part of the thesis contained the comparison of super cell energies of the ATLAS main readout and the demonstrator readout. The studies have shown, that the energy reconstruction for the demonstrator is satisfying but also that super cells with no energy deposit occur. The non-radiation hardness of the electronics in the front end crate might be the reason for that. In the analysis of the shower shape variables discrepancies in the distributions occurred because of the different digitization of the readout systems and due to data-intern restrictions on calorimeter cell information of the ATLAS main readout. Nevertheless the enhanced granularity with super cells is a great advantage compared to the readout with trigger towers. The distributions for the shower shape variables showed that jet and electron events can be well separated. Therefore, the differentiation of these particles will be improved within the Level-1 trigger.

In the last part of the thesis, pile-up at the demonstrator readout was investigated. It was shown that the mean pile-up exhibits a distribution that depends on the position of the bunch crossing in the bunch train. At the beginning of a bunch train we can

7. Summary and Outlook

see a positive mean pile-up energy, which decreases to zero and stays there until the end of the bunch train. Bunch crossings in between two bunch trains have a negative mean pile-up energy. The pile-up correlates with the instantaneous luminosity, which could be shown in the time spectrum of the mean pile-up. The single pile-up event spectrum will need further investigations in order to provide information on pile-up correction. Especially the deconvolution of the energy resolution must be object of further investigations.

At the beginning of 2018 the french LAr trigger digitizer board was replaced and a new firmware, "LAr Trigger prOcessing MEzzanine" (LATOME) was installed. This provides new data with an revised readout, which will be object of further investigations. Optimizing the energy reconstruction is an ongoing important task. Instead of the Optimal Filter different filter algorithms like the "Wiener Filter" could be applied and investigated.

A. Examined Runs

The following table lists the examined runs that were basis for the analysis of this thesis. The first column contains the run number. The second column displays the amount of successful matched events relative to the whole number of events in the file. In the third column the total number of matched events is shown. The last column comprises the number of matched events, which fulfill the in section 4.5 described condition in equation 4.11.

Runnumber	Matching / %	Matched events	Events with dS_max ≤ 10
330025	99.9	58,356	58,082
330074	99.8	13,382	13,309
330079	99.8	15,188	15,111
330160	98	6,065	6,019
330166	100	2,293	2,290
330203	99.9	97,132	95,570
330294	99.9	87,913	87,578
330328	99.9	38,465	3,220
330470	99.9	15,075	14,995
330857	100	333	333
330874	100	6	6
330875	100	857	857
331019	99.8	562	559
331033	99.9	4,642	4,610
331082	96.8	1,380	1,368
331085	99.9	106,606	106,218
331129	99.8	17,257	17,136
331215	99.8	12,682	12,632
331462	99.9	10,489	10,414
331466	99.9	18,461	18,395
331479	99.9	23,656	22,531
331697	99.9	18,347	18,192
331710	99.9	31,536	31,409
331742	99.9	93,890	44,888
331772	99.9	9,783	9,752
331905	99.9	7,481	7,444
331951	99.9	15,678	15,578
332896	100	9,117	9,073
332915	99.9	31,448	31,300
332955	100	16,632	16,538
333192	99.9	28,633	10,737
333367	99.9	13,014	12,993
333426	99.9	12,065	12,036
333487	99.9	62,125	61,980
333519	99.9	10,941	10,892
333707	99.9	3,246	3,221
333828	99.9	52,846	52,673
333853	99.9	13,467	13,404
333994	99.9	3,070	3,045
334264	99.9	44,119	43,763
334350	99.9	59,311	59,092
334384	99.9	6,937	6,896
334413	99.9	70,923	70,689
334487	99.9	66,323	65,644
334580	99.9	3,784	3,747
334637	99.9	32,603	32,446
334710	99.9	33,964	33,787
334849	99.9	26,094	26,010

334960	99.9	75,572	75,307
334993	99.9	56,273	56,095
335016	99.9	959	950
335022	99	45,329	45,068
335056	100	792	792
335082	100	719	713
335131	99.9	15,436	15,322
335170	99.9	53,416	53,177
335282	100	1,994	1,985
336782	99.9	85,679	85,386
336915	99.9	50,369	44,795
336927	99.9	77,730	77,406
336944	99.9	25,354	25,216
336998	99.9	27,624	27,461
337005	98.8	21,881	21,760
337107	99.8	61,713	61,429
337156	97	10,610	10,537
338183	99.9	78,246	77,750
338220	99.9	103,118	102,527
338259	99.8	55,925	45,050
338263	99.6	76,833	72,502
338349	99.7	87,888	86,593
338377	96	70,300	62,664
338480	99.7	71,304	70,698
338498	99.3	61,457	61,062
338608	74.6	43,162	42,841
338712	97.8	69,030	67,462
338834	98.5	8,963	8,905
338897	99	61,262	60,928
338933	99.9	70,813	70,180
338987	99.9	90,328	89,711
339346	99.3	6,389	6,336
339387	99.8	46,627	46,285
339396	99.7	21,787	21,617
339562	99.9	3,181	3,155
339758	99.9	91,694	87,683

Sum

3,037,934

2,885,810

B. Mean Pile-up per SC

Figure B.1 displays the mean energy deposit of all pile-up events per BC in ADC counts for two different SCs in the middle layer.

As explained in section 6.1, at the beginning of the two bunch trains peaks are visible. For the upper plots, beyond the peak the distributions approach the pedestal value. For the lower plots, since the pedestal was subtracted, the distribution gets close to zero. In between the two bunch trains the distributions drop. In BCs before the first bunch train, the distribution gets close to zero as well, because no pp collisions and therefore, no pile-up take place. The figures show that the calibrated pedestal value is close to the mean pile-up in the region of pile-up compensation.

B. Mean Pile-up per SC

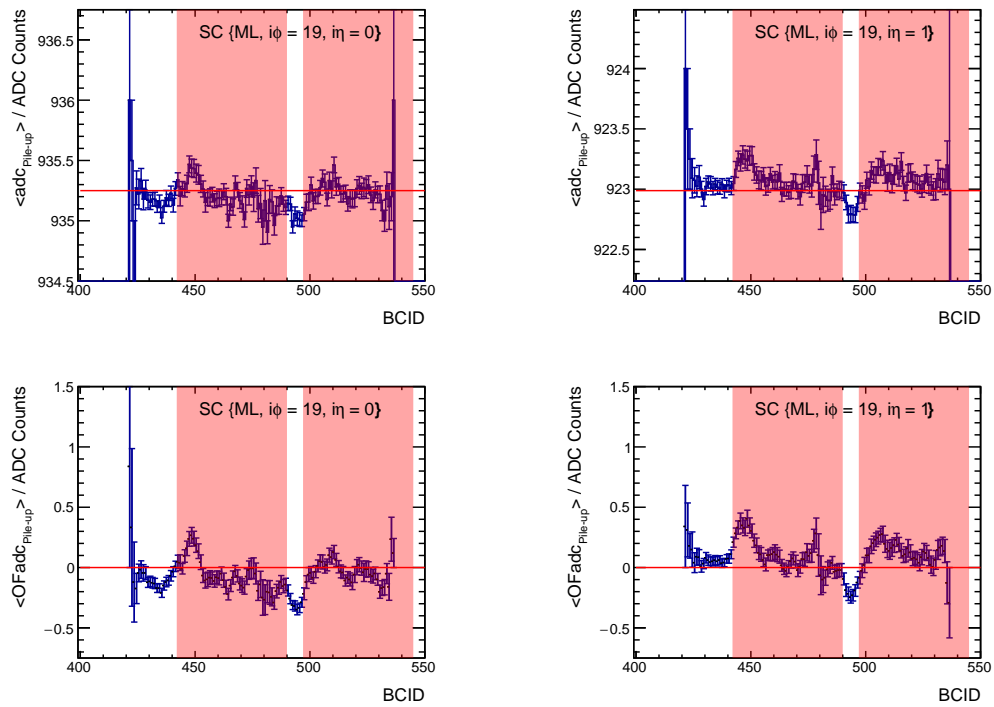


Figure B.1: Mean energy deposit of all pile-up events per BC of two different SCs in the middle layer for run 332896. The upper plots show mean ADC counts, whereas in the lower plots, the pedestal value is subtracted and the OF is applied. The highlighted regions in red indicate filled bunches. The horizontal red line displays the pedestal value.

Acronyms

ABBA	ATCA Board for a Baseline of liquid argon Acquisition
ADC	Analog-to-Digital Converter
ALFA	Absolute Luminosity For ATLAS
ALICE	A Large Ion Collider Experiment
AOD	Analysis Object Data
ATLAS	A Toroidal LHC ApparatuS
BC	Bunch Crossing
BCID	Bunch Crossing Identification
BNL	Brookhaven National Laboratory
CERN	Conseil européen pour la recherche nucléaire
CMS	Compact Muon Solenoid
CNI	Coulomb-Nuclear Interference
CP	Cluster Processor
CTP	Central Trigger Processor
DAQ	Data Acquisition
EC	Event Counter
ECRC	Event Counter Reset Counter
eFEX	electromagnetic Feature Extractor
EM	Electromagnetic
EMB	Electromagnetic Barrel Calorimeter
EMEC	Electromagnetic Endcap Calorimeter
ESD	Event Summary Data
FCal	Forward Calorimeter
FEB	Front End Board

Acronyms

FEC	Front End Crate
FPGA	Field Programmable Gate Array
FTK	Fast Tracker
HEC	Hadronic Endcap Calorimeter
HLT	High Level Trigger
JEP	Jet/Energy-sum Processor
jFEX	Jet Feature Extractor
L1	Level-1
L1A	Level-1 accept
L1Calo	Level-1 calorimeter trigger
L1ID	Level-1 Identification
L2	Level-2
LAL/Saclay	Laboratoire de l'accélérateur linéaire, Université Paris Saclay
LAr	Liquid Argon
LATOME	LAr Trigger prOcessing MEzzanine
LDPS	LAr Digital Processing System
LHC	Large Hadron Collider
LHCb	Large Hadron Collider beauty
LS	long shutdown
LS1	Long Shutdown 1
LS2	Long Shutdown 2
LS3	Long Shutdown 3
LSB	Layer Sum Board
LTDB	LAr Trigger Digitizer Board
OF	Optimal Filter
PP	Pre-Processor
pp	proton-proton
QCD	Quantum Chromodynamics
QED	Quantum Electrodynamics

ROD	Readout Driver
ROI	Region of Interest
SC	Super Cell
SC ID	Supercell Identification
SCA	Switched Capacitor Array
SM	Standard Model
SSV	Shower Shape Variable
TBB	Tower Builder Board
TRT	Transition Radiation Tracker
TT	Trigger Tower
TTC	trigger, timing and control
TType	Trigger Type

Bibliography

- [1] S.L. Glashow, Nucl. Phys. **22** (1961) 579;
S. Weinberg, Phys. Rev. Lett. **19** (1967) 1264;
A. Salam, *Elementary Particle Theory*, Ed. N. Svartholm, Stockholm, *Almqvist and Wiksell*, 1968, p. 367;
G. t'Hooft, Nucl. Phys. **B 35** (1971) 167;
G. t'Hooft and M. Veltman, Nucl. Phys. **B 44** (1972) 189.
H. Fritzsch, M. Gell-Mann, H. Leutwyler, Phys. Lett. **B 47** (1973) 365;
H. D. Politzer, Phys. Rev. Lett. **30** (1973) 1346;
D. Gross, F. Wilczek, Phys. Rev. Lett. **30** (1973) 1343;
S. Weinberg, Phys. Rev. Lett. **31** (1973) 494.
- [2] J. R. Ellis, *Limits of the Standard Model*, Tech. Rep. hep-ph/0211168.
CERN-TH-2002-320, CERN, Geneva, Nov, 2002.
<http://cds.cern.ch/record/591472>.
- [3] L. Evans and P. Bryant, *LHC Machine*, Journal of Instrumentation **3** no. 08, (2008) S08001. <http://stacks.iop.org/1748-0221/3/i=08/a=S08001>.
- [4] ATLAS Collaboration, G. Aad et al., *The ATLAS Experiment at the CERN Large Hadron Collider*, JINST **3** (2008) S08003.
- [5] W. Commons, *Standard model of elementary particles*, 2007.
https://en.wikipedia.org/wiki/File:Standard_Model_of_Elementary_Particles.svg. Image.
- [6] D. Griffiths, *Introduction to Elementary Particles*, 2008. Wiley-VCH.
- [7] ATLAS Collaboration, G. Aad et al., *Observation of a new particle in the search for the Standard Model Higgs boson with the ATLAS detector at the LHC*, Phys. Lett. **B716** (2012) 1–29, arXiv:1207.7214 [hep-ex].
- [8] CMS Collaboration, S. Chatrchyan et al., *Observation of a new boson at a mass of 125 GeV with the CMS experiment at the LHC*, Phys. Lett. **B716** (2012) 30–61, arXiv:1207.7235 [hep-ex].

- [9] P.W. Higgs, Phys. Lett. **12** (1964) 132;
idem, Phys. Rev. Lett. **13** (1964) 508;
idem, Phys. Rev. **145** (1966) 1156;
F. Englert and R. Brout, Phys. Rev. Lett. **13** (1964) 321;
G.S. Guralnik, C.R. Hagen and T.W.B. Kibble, Phys. Rev. Lett **13** (1964) 585.
- [10] H. Wiedemann, *Particle Accelerator Physics*, 1993. Springer-Verlag Berlin Heidelberg New York.
- [11] C. Pralavorio, *Record luminosity: well done LHC*, ATLAS official page (2017).
<http://cds.cern.ch/record/2295027>.
- [12] B. J. Holzer, *Introduction to Particle Accelerators and their Limitations*,
arXiv:1705.09601 [physics.acc-ph].
http://inspirehep.net/record/1478540/files/1418884_29-50.pdf.
- [13] *The High-Luminosity LHC*, ATLAS official page (2015).
<http://cds.cern.ch/record/2114693>.
- [14] ATLAS Collaboration, *Summary plots from the ATLAS Standard Model physics group*, 2018. <https://atlas.web.cern.ch/Atlas/GROUPS/PHYSICS/CombinedSummaryPlots/SM/>.
- [15] S. Tavernier, *Interactions of Particles in Matter*, 2010.
https://doi.org/10.1007/978-3-642-00829-0_2.
- [16] K. Olive and P. D. Group, *Review of Particle Physics*, Chinese Physics C **38** no. 9, (2014) 090001. <http://stacks.iop.org/1674-1137/38/i=9/a=090001>.
- [17] M. Berger, *XCOM: Photon Cross Section Database (version 1.5)*, 2010.
<http://physics.nist.gov/xcom>. Accessed: 2018-06-26.
- [18] C. Leroy and P.-G. Rancoita, *Physics of cascading shower generation and propagation in matter: principles of high-energy, ultrahigh-energy and compensating calorimetry*, Reports on Progress in Physics **63** no. 4, (2000) 505.
<http://stacks.iop.org/0034-4885/63/i=4/a=202>.
- [19] The CMS Collaboration, S. Chatrchyan and G. Hmayakyan, *The CMS experiment at the CERN LHC*, Journal of Instrumentation **3** no. 08, (2008) S08004.
<http://stacks.iop.org/1748-0221/3/i=08/a=S08004>.
- [20] The LHCb Collaboration, A. A. A. Jr and L. M. A. Filho, *The LHCb Detector at the LHC*, Journal of Instrumentation **3** no. 08, (2008) S08005.
<http://stacks.iop.org/1748-0221/3/i=08/a=S08005>.

- [21] The ALICE Collaboration, K. Aamodt and A. A. Quintana, *The ALICE experiment at the CERN LHC*, Journal of Instrumentation **3** no. 08, (2008) S08002.
<http://stacks.iop.org/1748-0221/3/i=08/a=S08002>.
- [22] J. Haffner, *The CERN accelerator complex. Complexe des accélérateurs du CERN*, CERN (2013). <http://cds.cern.ch/record/1621894>. General Photo.
- [23] ATLAS Collaboration, *Radiofrequency cavities*, ATLAS official page (2012).
<http://cds.cern.ch/record/1997424>.
- [24] C. Chavez, *The ATLAS Trigger System*, 2015.
<https://indico.cern.ch/event/352570/contributions/828882/attachments/698279/958830/TriggerOverview-SCWS-Chile.pdf>.
- [25] ATLAS Collaboration, *ATLAS Run Bunch Group Set 1956*, 2017.
https://atlas-trigconf.cern.ch/bunchgroups/graphics/plots/bunchgroupset_1956.png.
- [26] Z. Marshall and the Atlas Collaboration, *Simulation of Pile-up in the ATLAS Experiment*, Journal of Physics: Conference Series **513** no. 2, (2014) 022024.
<http://stacks.iop.org/1742-6596/513/i=2/a=022024>.
- [27] *The HL-LHC project*, 2015.
<https://hilumilhcds.web.cern.ch/about/hl-lhc-project0>.
- [28] ATLAS Collaboration, *ATLAS Liquid Argon Calorimeter Phase-I Upgrade Technical Design Report*, Tech. Rep. CERN-LHCC-2013-017. ATLAS-TDR-022, Sep, 2013. <https://cds.cern.ch/record/1602230>. Final version presented to December 2013 LHCC.
- [29] ATLAS Collaboration, G. Aad et al., *Expected Performance of the ATLAS Experiment - Detector, Trigger and Physics*, CERN (2009), arXiv:0901.0512 [hep-ex].
- [30] J. Pequeno, *Computer generated image of the ATLAS Liquid Argon*, 2008.
<http://cds.cern.ch/record/1095928>.
- [31] *Particle detection in the subsystems of the ATLAS detector*, 2016.
<https://i1.wp.com/particlebites.com/wp-content/uploads/2016/10/atlas.jpg?ssl=1>. Image.
- [32] C. A. Lee, *Missing p_T Reconstruction at ATLAS*, Journal of Physics: Conference Series **645** no. 1, (2015) 012012.
<http://stacks.iop.org/1742-6596/645/i=1/a=012012>.

- [33] ATLAS Collaboration, C. Bernius, *The ATLAS Trigger algorithms upgrade and performance in Run 2*, Talk at Conference (2017).
<http://cds.cern.ch/record/2276781>.
- [34] T. Perez Cavalcanti, *The ATLAS High Level Trigger Steering Framework and the Trigger Configuration System.*, Tech. Rep. ATL-DAQ-PROC-2011-016, CERN, Geneva, Apr, 2011. <http://cds.cern.ch/record/1344815>.
- [35] H. Zhang and the ATLAS Liquid Argon Calorimeter Group, *The ATLAS Liquid Argon Calorimeter: Overview and Performance*, Journal of Physics: Conference Series **293** no. 1, (2011) 012044.
<http://stacks.iop.org/1742-6596/293/i=1/a=012044>.
- [36] N. D. Dayot, *Performance of the Demonstrator System for the Phase-I Upgrade of the Trigger Readout Electronics of the ATLAS Liquid Argon Calorimeters*, Journal of Instrumentation **11** no. 01, (2016) C01026.
<http://stacks.iop.org/1748-0221/11/i=01/a=C01026>.
- [37] H. Abreu and M. Aharrouche, *Performance of the electronic readout of the ATLAS liquid argon calorimeters*, Journal of Instrumentation **5** no. 09, (2010) P09003.
<http://stacks.iop.org/1748-0221/5/i=09/a=P09003>.
- [38] T. Schoerner-Sadenius, *The Trigger of the ATLAS Experiment. The trigger of the ATLAS experiment.*, Mod. Phys. Lett. A **18** no. hep-ex/0307078, (2003) 2149–2168. 21 p. <http://cds.cern.ch/record/630658>. Comments: 21 pages, 11 figures, submitted to Mod. Phys. Lett. A.
- [39] ATLAS Collaboration, G. Aad et al., *Technical Design Report for the Phase-I Upgrade of the ATLAS TDAQ System*, Tech. Rep. CERN-LHCC-2013-018. ATLAS-TDR-023, ATLAS, Sep, 2013. <https://cds.cern.ch/record/1602235>. Final version presented to December 2013 LHCC.
- [40] R. Schaffer and S. C. M. Bentvelsen, *Definition of Offline Readout Identifiers for the ATLAS detector*, Tech. Rep. ATL-SOFT-2001-004, CERN, Geneva, Feb, 2001. <http://cds.cern.ch/record/684167>. revised version number 1 submitted on 2001-05-28 13:21:00.
- [41] ATLAS Collaboration Collaboration, S. Staerz, *Electronics Development for the ATLAS Liquid Argon Calorimeter - Trigger and Readout for Future LHC Running -*, Talk at Conference (2016). <https://cds.cern.ch/record/2153167>.
- [42] ATLAS Collaboration, *LAr Demonstrator Twiki*, 2018.
<https://twiki.cern.ch/twiki/bin/view/LAr/LArDemonstrator>.
Accessed: 2018-05-09.

- [43] K. A. Assamagan and D. Barberis, *Final report of the ATLAS AOD/ESD Definition Task Force*, CDS (2004).
- [44] ATLAS Collaboration, A. Haas, *ATLAS Pileup and Overlay Simulation*, 2014. https://indico.cern.ch/event/279530/contributions/634995/attachments/511924/706533/Haas_ATLAS_PileupOverlay_3-19-2014.pdf#search=atlas%20zerobias.
- [45] ATLAS Collaboration, *Fast TracKer (FTK) Technical Design Report*, Tech. Rep. CERN-LHCC-2013-007. ATLAS-TDR-021, 2013. <https://cds.cern.ch/record/1552953>.
- [46] S. Jakobsen, *Performance evaluation and optimization of the luminosity detector ALFA*. PhD thesis, Bohr Inst., 2010. <http://inspirehep.net/record/886989/files/CERN-THESIS-2010-091.pdf>.
- [47] ATLAS Collaboration, F. Dudziak, *Electron reconstruction and identification in ATLAS. Implication for the Higgs into four electron final state*, CERN (2010) 499–504. <http://cdsweb.cern.ch/record/1275567/files/ATL-PHYS-PROC-2010-039.pdf>.
- [48] ATLAS Collaboration, *Official Isolation Working Points*, 2018. <https://twiki.cern.ch/twiki/bin/viewauth/AtlasProtected/IsolationSelectionTool>. Accessed: 2018-05-29.
- [49] ATLAS Collaboration, *Reconstruction and Identification of Electrons*, Tech. Rep. ATL-PHYS-PUB-2009-004. ATL-COM-PHYS-2009-170, CERN, Geneva, Apr, 2009. <http://cds.cern.ch/record/1171939>. CSC PUB Note.
- [50] ATLAS Collaboration, *ATLAS electron, photon and muon isolation in Run 2*, Tech. Rep. ATL-COM-PHYS-2017-290, CERN, Geneva, Mar, 2017. <https://cds.cern.ch/record/2256658>. This note contains the Moriond 2017 recommendations. It will be updated when new recommendations become available.
- [51] M. Cacciari, G. P. Salam, and G. Soyez, *The Anti- $k(t)$ jet clustering algorithm*, JHEP **04** (2008) 063, arXiv:0802.1189 [hep-ph].
- [52] W. Cleland and E. Stern, *Signal processing considerations for liquid ionization calorimeters in a high rate environment*, Nuclear Instruments and Methods in Physics Research Section A: Accelerators, Spectrometers, Detectors and Associated Equipment **338** no. 2, (1994) 467 – 497. <http://www.sciencedirect.com/science/article/pii/0168900294913323>.
- [53] Provided by M. Hils (maximilian.hils@cern.ch).

- [54] for the CMS Collaboration Collaboration, F. Sikler, *Towards the measurement of charged hadron spectra in CMS*, Tech. Rep. CMS-CR-2008-077, CERN, Geneva, Oct, 2008. <http://cds.cern.ch/record/1166334>.
- [55] ATLAS Collaboration, *Demonstrator Data Analysis*, 2017. <https://twiki.cern.ch/twiki/bin/view/LAr/DemonstratorDataAnalysis>. Accessed: 2018-05-09.

Danksagung

An dieser Stelle möchte ich mich herzlich bei all jenen bedanken, die mich während meines Studiums und meiner Masterarbeit unterstützt und begleitet haben.

Besonders bedanken möchte ich mich bei Prof. Dr. Arno Straessner, der es mir ermöglicht hat, das CERN zu besuchen, der für alle Fragen immer ein offenes Ohr hatte und bei Problemen neue Wege eröffnet hat.

Außerdem möchte ich mich bei der gesamten Elektronik-Gruppe des IKTP bedanken. Insbesondere bei Maximilian Hils, der mit mir gemeinsam an den Schwierigkeiten der Daten getüftelt hat, Nico Madysa, der scheinbar für wirklich alle computertechnischen Probleme eine Lösung zaubern kann und Philipp Horn, der für jegliche Fragen und Scherze ein offenes Ohr hatte.

Ein herzlicher Dank geht auch an alle Korrekturleser Maximilian Hils, Nico Madysa, Philipp Horn, Wolfgang Mader, Arno Straessner, Lukas Reimer und Jonathan Berthold.

Ein großer Dank geht an meine Familie. Ihr habt mich durch die letzten Jahre begleitet, mich unterstützt und in Phasen des Zweifels ermutigt. Jonathan, ich danke dir für deine Geduld, dein Zuhören und, dass du meine Arbeit tatsächlich verstehst.

Versicherung

Hiermit versichere ich, die vorliegende Arbeit selbständig, ohne fremde Hilfe und ohne Benutzung anderer als der von mir angegebenen Quellen angefertigt zu haben. Alle aus fremden Quellen direkt oder indirekt übernommenen Gedanken sind als solche gekennzeichnet. Die Arbeit wurde noch keiner Prüfungsbehörde in gleicher oder ähnlicher Form vorgelegt.

Dresden, 5. Juli 2018

Anne-Sophie Reimer